INTERNATIONAL JOURNAL FOR NUMERICAL METHODS IN FLUIDS, VOL. 14, 557–585 (1992)

MULTIVARIANT FINITE ELEMENTS FOR THREE-DIMENSIONAL SIMULATION OF VISCOUS INCOMPRESSIBLE FLOWS

MAHESH GUPTA,* TAI H. KWON† AND YOGESH JALURIA

Department of Mechanical and Aerospace Engineering, Rutgers, The State University of New Jersey, Piscataway, NJ 08855, U.S.A.

SUMMARY

Within multivariant elements, which have restricted degrees of freedom at some nodes, different velocity components have different variations. Shape functions for the multivariant elements $Q_1^+ P_0$ and $R_2^+ P_0$ are developed. With such shape functions the value of a velocity component within a multivariant element is shown to depend upon all the independent components of velocity at the nodes of the element.

The use of the $Q_1 P_0$ element to simulate flows with discontinuous boundary conditions generated disturbance throughout the flow domain, giving erroneous pressure and velocity distributions. The $Q_1^+ P_0$ element restricted the disturbance due to such discontinuities to a small region near the singular points, whereas the $R_2^+ P_0$ element completely eliminated the fluctuations. Flows with discontinuous boundary conditions were simulated with reasonable accuracy by partially relaxing the no-slip condition on the $Q_1 P_0$ elements near the singular points.

KEY WORDS Multivariant finite element Incompressible flow Pressure modes Shape functions

1. INTRODUCTION

Flow simulation of viscous incompressible materials using the finite element method has been an active topic of investigation for more than 20 years and is still a rapidly evolving subject. Various types of finite elements were used in the past to simulate such incompressible flows. Owing to a lack of understanding of the convergence properties of the elements used, erroneous results were obtained at times from many of these elements. It was discovered by Hood and Taylor[1,2] that equal-order interpolations for velocity and pressure give erroneous pressure distributions. They used interpolations for velocity one order higher than those for pressure to obtain better results. However, even with these mixed interpolations, difficulties were encountered in the pressure solution. For instance, the simplest of such mixed interpolations, using linear approximation for velocity (bilinear for two-dimensional quadrilateral elements and trilinear on three-dimensional brick elements) and piecewise constant approximation for pressure ($Q_1 P_0$),‡ gives acceptable

* Present address: Mechanical and Aerospace Engineering, Cornell University, Ithaca, NY 14853, U.S.A.
† Present address: Department of Mechanical Engineering, Pohang Institute of Science and Technology, South Korea.
‡ In the terminology used to name various finite element types, the first letter denotes the interpolation for velocity and the second letter denotes the interpolation for pressure. The subscripts specify the order of interpolation used. P_k means kth-order polynomial interpolation, whereas Q_k means kth-order polynomial interpolation in each direction.

0271–2091/92/050557–29$14.50

Received 28 September 1990
Revised 6 June 1991

velocities for certain combinations of boundary conditions and element distribution, but the pressure distribution obtained is afflicted with the checkerboard pressure mode.[3] A pressure distribution suffering from the checkerboard pressure mode exhibits large oscillations between neighbouring elements. The checkerboard pressure mode can be filtered out easily on a regular mesh by averaging the pressure over the neighbouring elements, but filtering this spurious pressure mode on a distorted mesh is a very complicated problem. Similar difficulties were encountered in the higher-order Q_kQ_{k-1} $(k>1)$ elements. Hood and Taylor used the P_2P_1 triangular element to obtain a reliable two-dimensional simulation of incompressible flows. Brezzi and Falk[4] and Stenberg[5] generalized it to the P_3P_2 element, which also gives results that are free of spurious pressure modes. The Q_lP_{l-1} elements, with $l>1$, were also found to lead to stable approximations to the velocity and pressure fields.

Pioneering work on the existence and uniqueness of the solution of the Navier–Stokes equation for incompressible flows was done by Babuška[6] and Brezzi.[7] They studied it as a saddle point problem arising from the Lagrangian multiplier approach. For the flow of incompressible fluids the Lagrangian multiplier is nothing but the pressure in the flow domain. Babuška and Brezzi introduced the compatibility condition to be satisfied by the velocity and pressure solution spaces. The Q_1P_0 and other higher-order Q_kQ_{k-1} $(k>1)$ elements do not satisfy the Babuška–Brezzi condition, which is why the pressure distribution obtained from these elements is generally afflicted with spurious pressure modes.

By enriching the lower-order standard elements, Fortin[8] introduced a series of new elements which satisfy the Babuška–Brezzi condition and are also computationally very efficient. The simplest member of the series, $Q_1^+P_0$ is derived from the Q_1P_0 (trilinear velocity and constant pressure) 'standard' brick element. The $Q_1^+P_0$ element is obtained by adding one velocity node on each of the six faces of the Q_1P_0 element (Figure 1). Each of the nodes on the faces has only one degree of freedom, which is the velocity component normal to the face. Owing to the restricted degree of freedom at the mid-face nodes, the $Q_1^+P_0$ element is multivariant in nature, i.e. different velocity components vary differently within the element. Velocity components parallel to one of the six faces of the $Q_1^+P_0$ element vary bilinearly over the face, whereas variation of the velocity component normal to a face is biquadratic over the face. The pressure is constant within a $Q_1^+P_0$ element. Another multivariant finite element, called $R_2^+P_0$, is shown in Figure 1(c). It is obtained from the $Q_1^+P_0$ element by adding one velocity node on each of the 12 edges. Each of these new nodes has only two degrees of freedom, which are the velocity components normal to the edge. Therefore on an $R_2^+P_0$ element the velocity components normal to an edge vary quadratically over the edge, whereas the velocity component along an edge varies linearly over the edge. The pressure is constant within an $R_2^+P_0$ element.

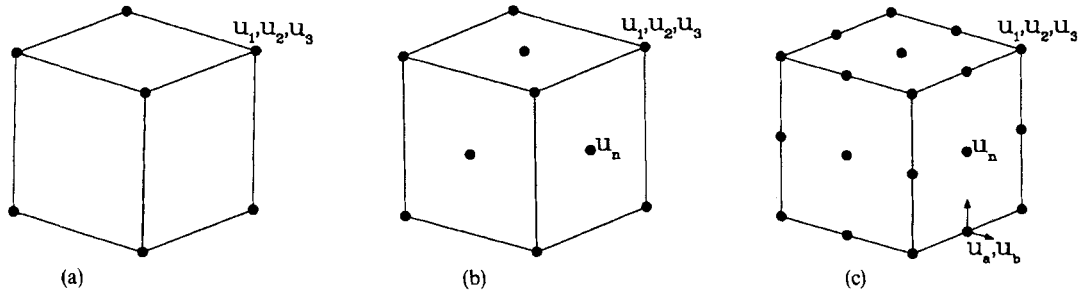

Figure 1. Three-dimensional finite elements: (a) Q_1P_0 element; (b) $Q_1^+P_0$ element; (c) $R_2^+P_0$ element

In the finite element method the velocity and pressure at a point inside an element are represented as a linear form in terms of the velocity and pressure values at the nodes:

$$\mathbf{u} = N_i \mathbf{u}_i, \tag{1}$$

$$p = N_i^{(p)} p_i, \tag{2}$$

where N_i are the velocity shape functions, $N_i^{(p)}$ are the pressure shape functions, $\mathbf{u}_i$ and p_i are the velocity and pressure respectively at the nodes of the element and $\mathbf{u}$ and p are the velocity and pressure respectively at a point inside the element.

Within the elements which have three degrees of freedom at all the velocity nodes, the three velocity components have identical variation (univariant elements). The value of a velocity component within a univariant element depends only upon the nodal values of the same velocity component. That is, the value of the velocity component is independent of the values of other components of velocity at the nodes. For instance, for the Q_1P_0 element, if u^x, u^y and u^z are the velocity components in the x-, y- and z-directions respectively, then

$$u^x = \sum_{i=1}^{\infty} N_i u_i^x, \qquad u^y = \sum_{i=1}^{\infty} N_i u_i^y, \qquad u^z = \sum_{i=1}^{\infty} N_i u_i^z, \tag{3}$$

where $i = 1, \ldots, 8$ correspond to the eight velocity nodes of the Q_1P_0 element and u_i^x, u_i^y and u_i^z are respectively the x-, y- and z-components of velocity at the ith node.

However, for the elements which have restricted degrees of freedom at some of the nodes, different components vary differently within the element (multivariant elements). For such elements within which different velocity components have different variations, each component of velocity depends upon the values of all independent velocity components at the nodes of the element. At a point inside a $Q_1^+P_0$ element

$$\begin{aligned} u^x &= \sum_{i=1}^{8} (N_i^{xx} u_i^x + N_i^{xy} u_i^y + N_i^{xz} u_i^z) + \sum_{i=9}^{14} N_i^x u_i^n, \\ u^y &= \sum_{i=1}^{8} (N_i^{yx} u_i^x + N_i^{yy} u_i^y + N_i^{yz} u_i^z) + \sum_{i=9}^{14} N_i^y u_i^n, \\ u^z &= \sum_{i=1}^{8} (N_i^{zx} u_i^x + N_i^{zy} u_i^y + N_i^{zz} u_i^z) + \sum_{i=9}^{14} N_i^z u_i^n, \end{aligned} \tag{4}$$

where $N_i^{\alpha\beta}$ $(\alpha, \beta = x, y, z)$ are the shape functions corresponding to the eight corner nodes, N_i^{α} $(\alpha = x, y, z)$ are the shape functions corresponding to the six mid-face nodes, u_i^x, u_i^y and u_i^z are respectively the x-, y- and z-components of velocity at the ith corner node and u_i^n is the normal component of velocity at the ith mid-face node.

Similarly, at a point inside an $R_2^+P_0$ element each velocity component depends upon the values of three components of velocity at the eight corner nodes, two velocity components at the 12 mid-edge nodes and the normal component of velocity at the six mid-face nodes. Therefore at a point inside an $R_2^+P_0$ element

$$\begin{aligned} u^x &= \sum_{i=1}^{8} (N_i^{xx} u_i^x + N_i^{xy} u_i^y + N_i^{xz} u_i^z) + \sum_{i=9}^{20} (N_i^{xa} u_i^{n1} + N_i^{xb} u_i^{n2}) + \sum_{i=21}^{26} N_i^x u_i^n, \\ u^y &= \sum_{i=1}^{8} (N_i^{yx} u_i^x + N_i^{yy} u_i^y + N_i^{yz} u_i^z) + \sum_{i=9}^{20} (N_i^{ya} u_i^{n1} + N_i^{yb} u_i^{n2}) + \sum_{i=21}^{26} N_i^y u_i^n, \\ u^z &= \sum_{i=1}^{8} (N_i^{zx} u_i^x + N_i^{zy} u_i^y + N_i^{zz} u_i^z) + \sum_{i=9}^{20} (N_i^{za} u_i^{n1} + N_i^{zb} u_i^{n2}) + \sum_{i=21}^{26} N_i^z u_i^n, \end{aligned} \tag{5}$$

where $N_i^{\alpha\beta}(\alpha = x, y, z; \beta = a, b)$ are the shape functions at the mid-edge nodes and u_i^{n1} and u_i^{n2} are the two velocity components normal to the edge at the ith mid-edge node.

For all the finite element types discussed in this paper, pressure is constant in the element. Therefore the pressure shape function is

$$N^{(p)} = 1.$$

Even for continuous pressure elements the pressure shape functions are quite straightforward. The velocity shape functions for the $Q_1^+ P_0$ and $R_2^+ P_0$ elements, which give the values of various terms in equations (4) and (5), are developed later in this paper. Shape functions for the $Q_1 P_0$ element are also included. Without any confusion the velocity shape functions are just referred to as shape functions. The natural co-ordinate system on a brick element, shown in Figure 2, is chosen so that the co-ordinate values on the faces of the brick are ± 1.

2. BASIC EQUATIONS FOR VISCOUS INCOMPRESSIBLE FLOW

For creeping flow of the generalized Newtonian fluid, neglecting the inertial and body forces, the momentum equation can be represented as

$$\operatorname{div}(2\mu\tilde{\varepsilon}) - \operatorname{grad} p = 0 \quad \text{in } \Omega. \tag{6}$$

Here μ is the viscosity of the fluid, p is the pressure, Ω is the flow domain in $\mathbb{R}^3$ and $\tilde{\varepsilon}$ is the strain rate tensor

$$\tilde{\varepsilon} = \tfrac{1}{2}[\operatorname{grad} \mathbf{u} + (\operatorname{grad} \mathbf{u})^{\mathrm{T}}], \tag{7}$$

where $\mathbf{u}$ is the velocity at a point in Ω. The incompressibility constraint can be represented as

$$\operatorname{div} \mathbf{u} = 0 \quad \text{in } \Omega. \tag{8}$$

The boundary conditions to be satisfied are

$$\mathbf{T} = \bar{\mathbf{T}} \quad \text{on } \Gamma_T, \tag{9}$$

$$\mathbf{u} = \bar{\mathbf{u}} \quad \text{on } \Gamma_u, \tag{10}$$

where $\mathbf{T}$ is the traction force at the boundary, Γ_T is the part of the boundary where the traction vector is given, Γ_u is the part of the boundary where the velocity is given, $\bar{\mathbf{T}}$ is the prescribed value of traction vector on Γ_T and $\bar{\mathbf{u}}$ is the prescribed value of velocity on Γ_u.

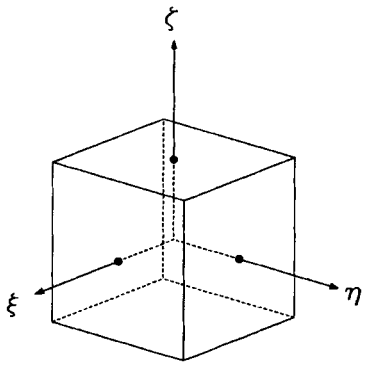

Figure 2. Natural co-ordinate system for a brick element

In order to obtain a variational form of the incompressible flow problem, we need to define the solution spaces for velocity and pressure. Defining on Ω the space of square integrable functions

$$L^2(\Omega)=\left\{u \,\middle|\, \int_\Omega |u(x)|^2 \,\mathrm{d}x<\infty\right\},$$

the Sobolov space

$$H^1(\Omega)=\{u|u\in L^2(\Omega),\ \operatorname{grad} u\in(L^2(\Omega))^3\}$$

and

$$V=(H^1(\Omega))^3,$$

we have the solution space of velocity

$$V_u=\{\mathbf{v}|\mathbf{v}\in V,\ \mathbf{v}=\bar{\mathbf{u}} \text{ on } \Gamma_u\}$$

and the solution space of pressure

$$Q=L^2(\Omega).$$

The variational form of the incompressible flow problem described in equations (6)–(10) is: find $(\mathbf{u}, p)\in V_u\times Q$ such that

$$\int_\Omega 2\mu\tilde{\boldsymbol{\varepsilon}}(\mathbf{u}):\tilde{\boldsymbol{\varepsilon}}(\mathbf{v})\,\mathrm{d}x-\int_\Omega p\operatorname{div}\mathbf{v}\,\mathrm{d}x=\int_\Gamma \bar{\mathbf{T}}\cdot\mathbf{v}\,\mathrm{d}s \quad \forall\mathbf{v}\in V_0, \tag{11}$$

$$\int_\Omega q\operatorname{div}\mathbf{u}\,\mathrm{d}x=0 \quad \forall q\in Q, \tag{12}$$

where

$$V_0=\{\mathbf{v}|\mathbf{v}\in V,\ \mathbf{v}=\mathbf{0} \text{ on } \Gamma_u\}.$$

According to the Babuška–Brezzi condition, for the existence of a unique solution to the variational form of the incompressible flow problem (equations (11) and (12)) there must exist a positive constant k such that

$$\sup_{\mathbf{v}\in V_0}\frac{\int_\Omega q\operatorname{div}\mathbf{v}\,\mathrm{d}x}{\|\mathbf{v}\|_V}\geqslant k\|q\|_{Q/\mathbb{R}} \qquad \forall q\in Q, \tag{13}$$

where

$$\|q\|_{Q/\mathbb{R}}=\inf_{c\in\mathbb{R}}\|q+c\|_Q$$

must be used since the pressure is defined only up to an additive constant.

Fortin[9] showed that the Babuška–Brezzi condition will be satisfied by a combination of discrete velocity and pressure solution spaces if for any given velocity field $\mathbf{v}\in V$ one can construct a vector field $\mathbf{v}_h$ in the discrete solution space of velocity such that

$$\int_\Omega \operatorname{div}(\mathbf{v}-\mathbf{v}_h)q_h\,\mathrm{d}x=0 \qquad \forall q_h\in Q_h, \tag{14}$$

$$\|\mathbf{v}_h\|_{H^1(\Omega)}\leqslant C\|\mathbf{v}\|_{H^1(\Omega)}, \tag{15}$$

with constant $C>0$ independent of h, the discretization factor. In equations (14) and (15) Q_h is the finite-dimensional solution space of pressure, q_h is an element of Q_h and $H^1(\Omega)$ is the Sobolov space.

In order to construct a discrete vector field on the $Q_1^+ P_0$ or $R_2^+ P_0$ element, which satisfies equation (14), the normal component of velocity at the six mid-face nodes must be determined by the equation

$$\int_{f_i} \mathbf{v}_h \mathrm{d}s = \int_{f_i} \mathbf{v} \mathrm{d}s, \qquad i=1, \ldots, 6, \tag{16}$$

where f_i, $i=1, \ldots, 6$, are the six faces of the element. Some of these interpolation operators are not in $H^1(\Omega)$ and hence do not satisfy equation (15). However, by using a local regularization operator described by Girault and Raviart,[10] a discrete velocity field satisfying both equations (14) and (15) can be constructed for the $Q_1^+ P_0$ as well as for the $R_2^+ P_0$ element. Therefore the $Q_1^+ P_0$ and $R_2^+ P_0$ elements both satisfy the Babuška–Brezzi condition.

3. SHAPE FUNCTIONS FOR $Q_1 P_0$ ELEMENT

The shape functions for the $Q_1 P_0$ element are given in most of the standard finite element books.[11,12] Using the variables

$$\xi_0 = \xi\xi_i, \qquad \eta_0 = \eta\eta_i, \qquad \zeta_0 = \zeta\zeta_i, \tag{17}$$

where ξ_i, η_i and ζ_i are the normalized co-ordinates of the ith node, the general expression for the shape function corresponding to the ith node of the $Q_1 P_0$ element is

$$N_i = \tfrac{1}{8}(1+\xi_0)(1+\eta_0)(1+\zeta_0). \tag{18}$$

4. SHAPE FUNCTIONS FOR $Q_1^+ P_0$ ELEMENT

In terms of the variables ξ_0, η_0 and ζ_0 the general expression for the shape function for the mid-face nodes of the $Q_1^+ P_0$ element is

$$N_i = \tfrac{1}{2}(1+\xi_0+\eta_0+\zeta_0)(1-\xi^2+\xi_0^2)(1-\eta^2+\eta_0^2)(1-\zeta^2+\zeta_0^2). \tag{19}$$

For the corner nodes of the $Q_1^+ P_0$ element the general expression for the shape function is

$$N_i = \tfrac{1}{8}(1+\xi_0)(1+\eta_0)(1+\zeta_0)[2(\xi_0+\eta_0+\zeta_0-1)-\xi_0\eta_0-\eta_0\zeta_0-\xi_0\zeta_0]. \tag{20}$$

However, these shape functions cannot be used as the reference shape functions for the $Q_1^+ P_0$ element because the normal vector at a mid-face node of the reference element does not remain normal to the corresponding face of the actual element in the global co-ordinate system.

On the $Q_1^+ P_0$ element we want the velocity components tangential to a face to vary bilinearly over the face and the velocity component normal to the face to vary biquadratically over the face. This can be achieved by separating the tangential and normal components of velocity at each of the six mid-face nodes of the $Q_1^+ P_0$ element. Using the shape functions presented in equations (19) and (20), the velocity within a $Q_1^+ P_0$ element is

$$\mathbf{u} = \sum_{i=1}^{8} N_i \mathbf{u}_i + \sum_{i=9}^{14} N_i \mathbf{u}_i,$$

where $i=1, \ldots, 8$ correspond to the eight corner nodes, $i=9, \ldots, 14$ correspond to the six mid-face nodes and $\mathbf{u}_i$ is the velocity at the ith node.

By separating the normal and tangential components of velocity at the mid-face nodes, we obtain

$$\mathbf{u}=\sum_{i=1}^{8} N_i\mathbf{u}_i+\sum_{i=9}^{14} N_i\{[\mathbf{u}_i-(\mathbf{u}_i\cdot\mathbf{n}_i)\mathbf{n}_i]+(\mathbf{u}_i\cdot\mathbf{n}_i)\mathbf{n}_i\}, \tag{21}$$

where $\mathbf{n}_i$ is the unit vector normal to the face at the ith mid-face node.

Since the velocity components tangential to a face of a $Q_1^+ P_0$ element vary bilinearly over the face, the value of the tangential velocity components at the mid-face node can be represented in terms of their values at the four nodes at the corners of the face. Thus

$$\mathbf{u}=\sum_{i=1}^{8} N_i\mathbf{u}_i+\sum_{i=9}^{14} N_i\left(\tfrac{1}{4}\sum_{c=1}^{4}[\mathbf{u}_c-(\mathbf{u}_c\cdot\mathbf{n}_i)\mathbf{n}_i]\right)+\sum_{i=9}^{14} N_i(\mathbf{u}_i\cdot\mathbf{n}_i)\mathbf{n}_i, \tag{22}$$

where $c=1,\ldots,4$ denote the nodes at the corners of the face on which the ith ($i=9,\ldots,14$) mid-face node is located and $\mathbf{u}_c$ is the velocity at the corner node c.

By interchanging the summations in the second term of equation (22), we obtain

$$\mathbf{u}=\sum_{i=1}^{8} N_i\mathbf{u}_i+\sum_{i=1}^{8}\sum_{f=1}^{3}\frac{N_f}{4}[\mathbf{u}_i-(\mathbf{u}_i\cdot\mathbf{n}_f)\mathbf{n}_f]+\sum_{i=9}^{14} N_i(\mathbf{u}_i\cdot\mathbf{n}_i)\mathbf{n}_i, \tag{23}$$

where $f=1,\ldots,3$ correspond to the mid-face nodes adjacent to the ith ($i=1,\ldots,8$) corner node, $\mathbf{n}_f$ is the unit vector normal to the face at the mid-face node f and N_f is the shape function for the mid-face node f (equation (19)).

By combining the first two terms in equation (23), we obtain the expressions for the three components of velocity within a $Q_1^+ P_0$ element:

$$\begin{aligned} u^x=&\sum_{i=1}^{8}\left(N_i+\sum_{f=1}^{3}\frac{N_f}{4}[1-(n_f^x)^2]\right)u_i^x-\sum_{i=1}^{8}\left(\sum_{f=1}^{3}\frac{N_f}{4}n_f^x n_f^y\right)u_i^y\\ &-\sum_{i=1}^{8}\left(\sum_{f=1}^{3}\frac{N_f}{4}n_f^x n_f^z\right)u_i^z+\sum_{i=9}^{14}N_i n_i^x u_i^n, \end{aligned} \tag{24}$$

$$\begin{aligned} u^y=&-\sum_{i=1}^{8}\left(\sum_{f=1}^{3}\frac{N_f}{4}n_f^x n_f^y\right)u_i^x+\sum_{i=1}^{8}\left(N_i+\sum_{f=1}^{3}\frac{N_f}{4}[1-(n_f^y)^2]\right)u_i^y\\ &-\sum_{i=1}^{8}\left(\sum_{f=1}^{3}\frac{N_f}{4}n_f^y n_f^z\right)u_i^z+\sum_{i=9}^{14}N_i n_i^y u_i^n, \end{aligned} \tag{25}$$

$$\begin{aligned} u^z=&-\sum_{i=1}^{8}\left(\sum_{f=1}^{3}\frac{N_f}{4}n_f^x n_f^z\right)u_i^x-\sum_{i=1}^{8}\left(\sum_{f=1}^{3}\frac{N_f}{4}n_f^y n_f^z\right)u_i^y\\ &+\sum_{i=1}^{8}\left(N_i+\sum_{f=1}^{3}\frac{N_f}{4}[1-(n_f^z)^2]\right)u_i^z+\sum_{i=9}^{14}N_i n_i^z u_i^n, \end{aligned} \tag{26}$$

where u^x, u^y and u^z are respectively the x-, y- and z-components of velocity at a point inside a $Q_1^+ P_0$ element, n_f^x, n_f^y and n_f^z are respectively the x-, y- and z-components of the unit vector normal to the face at the mid-face node f and u_i^x, u_i^y and u_i^z are respectively the x-, y- and z-components of velocity at the ith node.

Equations (24)–(26) give the values of various terms in equation (4). The shape functions in equations (24)–(26), which have different variations for different velocity components, will be called multivariant shape functions, whereas the shape functions given in equations (19) and (20),

which have same variation for all three velocity components, will be called univariant shape functions.

Next we are interested in finding the shape functions for the $R_2^+ P_0$ element. However, the shape functions for the $R_2 P_0$ element are presented first since they are required for the derivation of the shape functions for the $R_2^+ P_0$ element.

5. SHAPE FUNCTIONS FOR $R_2 P_0$ ELEMENT

An $R_2 P_0$ element (Figure 3) has velocity nodes at the eight corners and on each of the 12 edges of the brick element. The eight corner nodes have all three degrees of freedom, whereas each of the 12 mid-edge nodes has only two degrees of freedom, which are the velocity components normal to the edge.

The following equation gives the univariant shape functions for the corner nodes of the $R_2 P_0$ element:

$$N_i = \tfrac{1}{8}(1+\xi_0)(1+\eta_0)(1+\zeta_0)(\xi_0+\eta_0+\zeta_0-2). \tag{27}$$

The univariant shape functions for the mid-edge nodes of the $R_2 P_0$ element are

$$N_i = \tfrac{1}{4}(1+\xi_0)(1+\eta_0)(1+\zeta_0)(1-\xi^2+\xi_0^2)(1-\eta^2+\eta_0^2)(1-\zeta^2+\zeta_0^2). \tag{28}$$

Since the velocity components normal to an edge of the reference element do not remain normal to the edge after transformation to the global reference frame, to find the multivariant shape functions for the $R_2 P_0$ element, the velocity vector at the mid-edge nodes is decomposed into normal and tangential components and different interpolations are used for the normal and tangential components. Using the shape functions given in equations (27) and (28), the velocity at a point inside the $R_2 P_0$ element can be represented as

$$\mathbf{u} = \sum_{i=1}^{8} N_i \mathbf{u}_i + \sum_{i=9}^{20} N_i \mathbf{u}_i, \tag{29}$$

where $i = 1, \ldots, 8$ correspond to the eight corner nodes and $i = 9, \ldots, 20$ correspond to the 12 mid-edge nodes. By separating the tangential and normal velocity components at the mid-edge nodes, we obtain

$$\mathbf{u} = \sum_{i=1}^{8} N_i \mathbf{u}_i + \sum_{i=9}^{20} N_i \{[\mathbf{u}_i - (\mathbf{u}_i \cdot \mathbf{n}_{1i})\mathbf{n}_{1i} - (\mathbf{u}_i \cdot \mathbf{n}_{2i})\mathbf{n}_{2i}] + (\mathbf{u}_i \cdot \mathbf{n}_{1i})\mathbf{n}_{1i} + (\mathbf{u}_i \cdot \mathbf{n}_{2i})\mathbf{n}_{2i}\}, \tag{30}$$

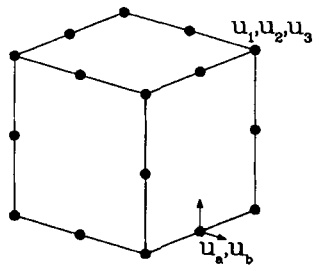

Figure 3. An $R_2 P_0$ element

where $\mathbf{n}_{1i}$ and $\mathbf{n}_{2i}$ are the two orthonormal vectors perpendicular to the edge at the ith mid-edge node.

Since the velocity component tangential to an edge of an R_2P_0 element varies linearly along the edge, the value of the tangential velocity component at the mid-edge node can be represented in terms of its value at the corner nodes at the two ends of the edge:

$$\mathbf{u}=\sum_{i=1}^{8} N_i\mathbf{u}_i+\sum_{i=9}^{20} N_i\left(\tfrac{1}{2}\sum_{c=1}^{2}[\mathbf{u}_c-(\mathbf{u}_c\cdot\mathbf{n}_{1i})\mathbf{n}_{1i}-(\mathbf{u}_c\cdot\mathbf{n}_{2i})\mathbf{n}_{2i}]\right)+\sum_{i=9}^{20} N_i[(\mathbf{u}_i\cdot\mathbf{n}_{1i})\mathbf{n}_{1i}+(\mathbf{u}_i\cdot\mathbf{n}_{2i})\mathbf{n}_{2i}], \tag{31}$$

where $c=1,2$ correspond to the corner nodes at the two ends of the edge on which the ith mid-edge node is located and $\mathbf{u}_c$ is the velocity at the corner node c.

By interchanging the summations in the second term of equation (31), we obtain

$$\mathbf{u}=\sum_{i=1}^{8} N_i\mathbf{u}_i+\sum_{i=1}^{8}\sum_{e=1}^{3}\frac{N_e}{2}[\mathbf{u}_i-(\mathbf{u}_i\cdot\mathbf{n}_{1e})\mathbf{n}_{1e}-(\mathbf{u}_i\cdot\mathbf{n}_{2e})\mathbf{n}_{2e}]+\sum_{i=9}^{20} N_i u_i^{n1}\mathbf{n}_{1i}+\sum_{i=9}^{20} N_i u_i^{n2}\mathbf{n}_{2i}, \tag{32}$$

where $e=1,\ldots,3$ correspond to the three mid-edge nodes adjacent to the ith corner node, $u_i^{n1}=\mathbf{u}_i\cdot\mathbf{n}_{1i}$ and $u_i^{n2}=\mathbf{u}_i\cdot\mathbf{n}_{2i}$. By combining the first two terms in equation (32), we obtain the expressions for the three velocity components in an R_2P_0 element:

$$\begin{aligned}u^x=&\sum_{i=1}^{8}\left(N_i+\sum_{e=1}^{3}\frac{N_e}{2}[1-(n_{1e}^x)^2-(n_{2e}^x)^2]\right)u_i^x-\sum_{i=1}^{8}\sum_{e=1}^{3}\frac{N_e}{2}(n_{1e}^x n_{1e}^y+n_{2e}^x n_{2e}^y)u_i^y\\&-\sum_{i=1}^{8}\sum_{e=1}^{3}\frac{N_e}{2}(n_{1e}^x n_{1e}^z+n_{2e}^x n_{2e}^z)u_i^z+\sum_{i=9}^{20}(N_i n_{1i}^x)u_i^{n1}+\sum_{i=9}^{20}(N_i n_{2i}^x)u_i^{n2},\end{aligned} \tag{33}$$

$$\begin{aligned}u^y=&-\sum_{i=1}^{8}\sum_{e=1}^{3}\frac{N_e}{2}(n_{1e}^x n_{1e}^y+n_{2e}^x n_{2e}^y)u_i^x+\sum_{i=1}^{8}\left(N_i+\sum_{e=1}^{3}\frac{N_e}{2}[1-(n_{1e}^y)^2-(n_{2e}^y)^2]\right)u_i^y\\&-\sum_{i=1}^{8}\sum_{e=1}^{3}\frac{N_e}{2}(n_{1e}^y n_{1e}^z+n_{2e}^y n_{2e}^z)u_i^z+\sum_{i=9}^{20}(N_i n_{1i}^y)u_i^{n1}+\sum_{i=9}^{20}(N_i n_{2i}^y)u_i^{n2},\end{aligned} \tag{34}$$

$$\begin{aligned}u^z=&-\sum_{i=1}^{8}\sum_{e=1}^{3}\frac{N_e}{2}(n_{1e}^x n_{1e}^z+n_{2e}^x n_{2e}^z)u_i^x-\sum_{i=1}^{8}\sum_{e=1}^{3}\frac{N_e}{2}(n_{1e}^y n_{1e}^z+n_{2e}^y n_{2e}^z)u_i^y\\&+\sum_{i=1}^{8}\left(N_i+\sum_{e=1}^{3}\frac{N_e}{2}[1-(n_{1e}^z)^2-(n_{2e}^z)^2]\right)u_i^z+\sum_{i=9}^{20}(N_i n_{1i}^z)u_i^{n1}+\sum_{i=9}^{20}(N_i n_{2i}^z)u_i^{n2},\end{aligned} \tag{35}$$

where n_{ie}^x, n_{ie}^y and n_{ie}^z $(i=1,2)$ are respectively the x-, y- and z-components of the unit vectors normal to the edge at the mid-edge node e.

At the centre of a face of the R_2P_0 element the value of the univariant shape functions corresponding to the four corner nodes of the face is $N_i=-\frac{1}{4}$ and the value of the univariant shape functions corresponding to the four mid-edge nodes is $N_i=\frac{1}{2}$. Therefore the three components of velocity at the centre of a face of the R_2P_0 element are

$$\begin{aligned}u^x=&\sum_{c=1}^{4}\left(-\tfrac{1}{4}+\sum_{e=1}^{2}\tfrac{1}{4}[1-(n_{1e}^x)^2-(n_{2e}^x)^2]\right)u_c^x-\sum_{c=1}^{4}\sum_{e=1}^{2}\tfrac{1}{4}(n_{1e}^x n_{1e}^y+n_{2e}^x n_{2e}^y)u_c^y\\&-\sum_{c=1}^{4}\sum_{e=1}^{2}\tfrac{1}{4}(n_{1e}^x n_{1e}^y+n_{2e}^x n_{2e}^z)u_c^z+\sum_{e=1}^{4}\frac{n_{1e}^x}{2}u_e^{n1}+\sum_{e=1}^{4}\frac{n_{2e}^x}{2}u_e^{n2},\end{aligned} \tag{36}$$

$$u^y = -\sum_{c=1}^{4}\sum_{e=1}^{2} \tfrac{1}{4}(n_{1e}^x n_{1e}^y + n_{2e}^x n_{2e}^y)u_c^x + \sum_{c=1}^{4}\left(-\tfrac{1}{4} + \sum_{e=1}^{2} \tfrac{1}{4}[1-(n_{1e}^y)^2 - (n_{2e}^y)^2]\right)u_c^y$$
$$-\sum_{c=1}^{4}\sum_{e=1}^{2} \tfrac{1}{4}(n_{1e}^y n_{1e}^z + n_{2e}^y n_{2e}^z)u_c^z + \sum_{e=1}^{4} \frac{n_{1e}^y}{2} u_e^{n1} + \sum_{e=1}^{4} \frac{n_{2e}^y}{2} u_e^{n2}, \tag{37}$$

$$u^z = -\sum_{c=1}^{4}\sum_{e=1}^{2} \tfrac{1}{4}(n_{1e}^x n_{1e}^z + n_{2e}^x n_{2e}^z)u_c^x - \sum_{c=1}^{4}\sum_{e=1}^{2} \tfrac{1}{4}(n_{1e}^y n_{1e}^z + n_{2e}^y n_{2e}^z)u_c^y$$
$$+\sum_{c=1}^{4}\left(-\tfrac{1}{4} + \sum_{e=1}^{2} \tfrac{1}{4}[1-(n_{1e}^z)^2 - (n_{2e}^z)^2]\right)u_c^z + \sum_{e=1}^{4} \frac{n_{1e}^z}{2} u_e^{n1} + \sum_{e=1}^{4} \frac{n_{2e}^z}{2} u_e^{n2}. \tag{38}$$

In the next section these values of the three velocity components at the centre of the faces of the R_2P_0 element are used in the derivation of the shape functions for the $R_2^+P_0$ element.

6. SHAPE FUNCTIONS FOR $R_2^+P_0$ ELEMENT

At the mid-face nodes of the $R_2^+P_0$ element the univariant shape functions are the same as the biquadratic–linear shape functions used for the mid-face nodes of the $Q_1^+P_0$ element:

$$N_i = \tfrac{1}{2}(1+\xi_0+\eta_0+\zeta_0)(1-\xi^2+\xi_0^2)(1-\eta^2+\eta_0^2)(1-\zeta^2+\zeta_0^2). \tag{39}$$

In terms of the variables ξ_0, η_0 and ζ_0 the general expression for the univariant shape function at the mid-edge nodes of the $R_2^+P_0$ element is

$$N_i = \tfrac{1}{4}(1+\xi_0)(1+\eta_0)(1+\zeta_0)(1-\xi^2+\xi_0^2)(1-\eta^2+\eta_0^2)(1-\zeta^2+\zeta_0^2)(\xi_0+\eta_0+\zeta_0-1). \tag{40}$$

The general expression for the univariant shape function for the corner nodes of the $R_2^+P_0$ element is

$$N_i = \tfrac{1}{8}(1+\xi_0)(1+\eta_0)(1+\zeta_0)(1-\xi_0-\eta_0-\zeta_0+\xi_0\eta_0+\eta_0\zeta_0+\xi_0\zeta_0). \tag{41}$$

Using the same technique as for the $Q_1^+P_0$ and R_2P_0 elements, the multivariant shape functions for the $R_2^+P_0$ elements can be derived by separating the tangential and normal components of velocity at the mid-face and mid-edge nodes. Using the univariant shape functions given in equations (39)–(41), the velocity within an $R_2^+P_0$ element can be represented as

$$\mathbf{u} = \sum_{i=1}^{8} N_i\mathbf{u}_i + \sum_{i=9}^{20} N_i\mathbf{u}_i + \sum_{i=21}^{26} N_i\mathbf{u}_i,$$

where $i=1, \ldots, 8$ correspond to the eight corner nodes, $i=9, \ldots, 20$ correspond to the 12 mid-edge nodes and $i=21, \ldots, 26$ correspond to the six mid-face nodes.

By separating the normal and tangential velocity components at the mid-edge and the mid-face nodes, we obtain

$$\mathbf{u} = \sum_{i=1}^{8} N_i\mathbf{u}_i + \sum_{i=9}^{20} N_i\{[\mathbf{u}_i - (\mathbf{u}_i\cdot\mathbf{n}_{1i})\mathbf{n}_{1i} - (\mathbf{u}_i\cdot\mathbf{n}_{2i})\mathbf{n}_{2i}] + (\mathbf{u}_i\cdot\mathbf{n}_{1i})\mathbf{n}_{1i}$$
$$+(\mathbf{u}_i\cdot\mathbf{n}_{2i})\mathbf{n}_{2i}\} + \sum_{i=21}^{26} N_i\{[\mathbf{u}_i - (\mathbf{u}_i\cdot\mathbf{n}_i)\mathbf{n}_i] + (\mathbf{u}_i\cdot\mathbf{n}_i)\mathbf{n}_i\}. \tag{42}$$

Similar to the R_2P_0 element, the tangential velocity component at the mid-edge node of the $R_2^+P_0$ element can be represented in terms of its value at the nodes on the two ends of the edge:

$$\mathbf{u}=\sum_{i=1}^{8} N_i\mathbf{u}_i+\sum_{i=9}^{20} N_i\left(\tfrac{1}{2}\sum_{c=1}^{2}[\mathbf{u}_c-(\mathbf{u}_c\cdot\mathbf{n}_{1i})\mathbf{n}_{1i}-(\mathbf{u}_c\cdot\mathbf{n}_{2i})\mathbf{n}_{2i}]\right)$$
$$+\sum_{i=9}^{20} N_i(u_i^{n1}\mathbf{n}_{1i}+u_i^{n2}\mathbf{n}_{2i})+\sum_{i=21}^{26} N_iu_i^n\mathbf{n}_i+\sum_{i=21}^{26} N_i[\mathbf{u}_i-(\mathbf{u}_i\cdot\mathbf{n}_i)\mathbf{n}_i]. \tag{43}$$

By interchanging the summations in the second term of equation (43), we obtain

$$\mathbf{u}=\sum_{i=1}^{8} N_i\mathbf{u}_i+\sum_{i=1}^{8}\sum_{e=1}^{3}\frac{N_e}{2}\{[\mathbf{u}_i-(\mathbf{u}_i\cdot\mathbf{n}_{1e})\mathbf{n}_{1e}-(\mathbf{u}_i\cdot\mathbf{n}_{2e})\mathbf{n}_{2e}]\}$$
$$+\sum_{i=9}^{20} N_i(u_i^{n1}\mathbf{n}_{1i}+u_i^{n2}\mathbf{n}_{2i})+\sum_{i=21}^{26} N_iu_i^n\mathbf{n}_i+\sum_{i=21}^{26} N_i[\mathbf{u}_i-(\mathbf{u}_i\cdot\mathbf{n}_i)\mathbf{n}_i], \tag{44}$$

where the notation used is the same as that in equation (32).

The last term in equation (44) requires special attention. The velocity components tangential to the face at the mid-face nodes of the $R_2^+P_0$ element should be expressed in terms of the three velocity components at the four nodes at the corners of the face and the two velocity components normal to the edge at the mid-edge nodes on the four sides of the face. Using the expressions derived for the components of velocity at the centre of a face of the R_2P_0 element (equations (36–38)), the x-component of the last term in equation (44) is

$$\sum_{i=21}^{26} N_i[u_i^x-(\mathbf{u}_i\cdot\mathbf{n}_i)n_i^x]$$
$$=\sum_{i=21}^{26} N_i[u_i^x-(u_i^xn_i^x+u_i^yn_i^y+u_i^zn_i^z)n_i^x]$$
$$=\sum_{i=21}^{26} N_i\left\{\left[\sum_{c=1}^{4}\left(-\tfrac{1}{4}+\sum_{e=1}^{2}\tfrac{1}{4}[1-(n_{1e}^x)^2-(n_{2e}^x)^2]\right)u_c^x-\sum_{c=1}^{4}\sum_{e=1}^{2}\tfrac{1}{4}(n_{1e}^xn_{1e}^y+n_{2e}^xn_{2e}^y)u_c^y\right.\right.$$
$$\left.-\sum_{c=1}^{4}\sum_{e=1}^{2}\tfrac{1}{4}(n_{1e}^xn_{1e}^z+n_{2e}^xn_{2e}^z)u_c^z+\sum_{e=1}^{4}\frac{n_{1e}^x}{2}u_e^{n1}+\sum_{e=1}^{4}\frac{n_{2e}^x}{2}u_e^{n2}\right]$$
$$-\left[\sum_{c=1}^{4}\left(-\tfrac{1}{4}+\sum_{e=1}^{2}\tfrac{1}{4}[1-(n_{1e}^x)^2-(n_{2e}^x)^2]\right)u_c^x-\sum_{c=1}^{4}\sum_{e=1}^{2}\tfrac{1}{4}(n_{1e}^xn_{1e}^y+n_{2e}^xn_{2e}^y)u_c^y\right.$$
$$\left.-\sum_{c=1}^{4}\sum_{e=1}^{2}\tfrac{1}{4}(n_{1e}^xn_{1e}^z+n_{2e}^xn_{2e}^z)u_c^z+\sum_{e=1}^{4}\frac{n_{1e}^x}{2}u_e^{n1}+\sum_{e=1}^{4}\frac{n_{2e}^x}{2}u_e^{n2}\right](n_i^x)^2$$
$$-\left[-\sum_{c=1}^{4}\sum_{e=1}^{2}\tfrac{1}{4}(n_{1e}^xn_{1e}^y+n_{2e}^xn_{2e}^y)u_c^x+\sum_{c=1}^{4}\left(-\tfrac{1}{4}+\sum_{e=1}^{2}\tfrac{1}{4}[1-(n_{1e}^y)^2-(n_{2e}^y)^2]\right)u_c^y\right.$$
$$\left.-\sum_{c=1}^{4}\sum_{e=1}^{2}\tfrac{1}{4}(n_{1e}^yn_{1e}^z+n_{2e}^yn_{2e}^z)u_c^z+\sum_{e=1}^{4}\frac{n_{1e}^y}{2}u_e^{n1}+\sum_{e=1}^{4}\frac{n_{2e}^y}{2}u_e^{n2}\right]n_i^xn_i^y$$
$$-\left[-\sum_{c=1}^{4}\sum_{e=1}^{2}\tfrac{1}{4}(n_{1e}^xn_{1e}^z+n_{2e}^xn_{2e}^z)u_c^x-\sum_{c=1}^{4}\sum_{e=1}^{2}\tfrac{1}{4}(n_{1e}^yn_{1e}^z+n_{2e}^yn_{2e}^z)u_c^y\right.$$
$$\left.\left.+\sum_{c=1}^{4}\left(-\tfrac{1}{4}+\sum_{e=1}^{2}\tfrac{1}{4}[1-(n_{1e}^z)^2-(n_{2e}^z)^2]\right)u_c^z+\sum_{e=1}^{4}\frac{n_{1e}^z}{2}u_e^{n1}+\sum_{e=1}^{4}\frac{n_{2e}^z}{2}u_e^{n2}\right]n_i^xn_i^z\right\}, \tag{45}$$

where in $\sum_{i=21}^{26} \cdots \sum_{c=1}^{4} \cdots \sum_{e=1}^{2} \cdots$, $i=21, \ldots, 26$ correspond to the six mid-face nodes, with $c=1, \ldots, 4$ denoting the associated four corner nodes for each of these faces and $e=1, 2$ corresponding to the two mid-edge nodes on the face with the ith mid-face node, which are adjacent to the corner node c, whereas in $\sum_{i=21}^{26} \cdots \sum_{e=1}^{4} \cdots$, $e=1, \ldots, 4$ correspond to the mid-edge nodes on the four sides of the face on which the ith mid-face node is located.

The x-component of velocity at a point inside an $R_2^+ P_0$ element can be obtained by collecting the terms for each degree of freedom in equations (44) and (45):

$$
\begin{aligned}
u^x = & \sum_{i=1}^{8} \left\{ N_i + \sum_{e=1}^{3} \frac{N_e}{2} [1-(n_{1e}^x)^2-(n_{2e}^x)^2] + \sum_{f=1}^{3} N_f \left[\left(-\tfrac{1}{4} + \sum_{e=1}^{2} \tfrac{1}{4}[1-(n_{1e}^x)^2-(n_{2e}^x)^2] \right)[1-(n_f^x)^2] \right.\right. \\
& \left.\left. + \sum_{e=1}^{2} \tfrac{1}{4}(n_{1e}^x n_{1e}^y + n_{2e}^x n_{2e}^y) n_f^x n_f^y + \sum_{e=1}^{2} \tfrac{1}{4}(n_{1e}^x n_{1e}^z + n_{2e}^x n_{2e}^z) n_f^x n_f^z \right] \right\} u_i^x \\
& + \sum_{i=1}^{8} \left\{ -\sum_{e=1}^{3} \frac{N_e}{2} (n_{1e}^x n_{1e}^y + n_{2e}^x n_{2e}^y) + \sum_{f=1}^{3} N_f \left[-\sum_{e=1}^{2} \tfrac{1}{4}(n_{1e}^x n_{1e}^y + n_{2e}^x n_{2e}^y)[1-(n_f^x)^2] \right.\right. \\
& \left.\left. -\left(-\tfrac{1}{4} + \sum_{e=1}^{2} \tfrac{1}{4}[1-(n_{1e}^y)^2-(n_{2e}^y)^2] \right) n_f^x n_f^y + \sum_{e=1}^{2} \tfrac{1}{4}(n_{1e}^y n_{1e}^z + n_{2e}^y n_{2e}^z) n_f^x n_f^z \right] \right\} u_i^y \\
& + \sum_{i=1}^{8} \left\{ -\sum_{e=1}^{3} \frac{N_e}{2} (n_{1e}^x n_{1e}^z + n_{2e}^x n_{2e}^z) + \sum_{f=1}^{3} N_f \left[-\sum_{e=1}^{2} \tfrac{1}{4}(n_{1e}^x n_{1e}^z + n_{2e}^x n_{2e}^z)[1-(n_f^x)^2] \right.\right. \\
& \left.\left. + \sum_{e=1}^{2} \tfrac{1}{4}(n_{1e}^y n_{1e}^z + n_{2e}^y n_{2e}^z) n_f^x n_f^y - \left(-\tfrac{1}{4} + \sum_{e=1}^{2} \tfrac{1}{4}[1-(n_{1e}^z)^2-(n_{2e}^z)^2] \right) n_f^x n_f^z \right] \right\} u_i^z \\
& + \sum_{i=9}^{20} \left(N_i n_{1i}^x + \sum_{f=1}^{2} \frac{N_f}{2} \{ n_{1i}^x [1-(n_f^x)^2] - n_{1i}^y n_f^x n_f^y - n_{1i}^z n_f^x n_f^z \} \right) u_i^{n1} \\
& + \sum_{i=9}^{20} \left(N_i n_{2i}^x + \sum_{f=1}^{2} \frac{N_f}{2} \{ n_{2i}^x [1-(n_f^x)^2] - n_{2i}^y n_f^x n_f^y - n_{2i}^z n_f^x n_f^z \} \right) u_i^{n2} + \sum_{i=21}^{26} (N_i n_i^x) u_i^n. \qquad (46)
\end{aligned}
$$

Similarly, the y- and z-components of velocity within an $R_2^+ P_0$ element are

$$
\begin{aligned}
u^y = & \sum_{i=1}^{8} \left\{ -\sum_{e=1}^{3} \frac{N_e}{2} (n_{1e}^x n_{1e}^y + n_{2e}^x n_{2e}^y) + \sum_{f=1}^{3} N_f \left[-\left(-\tfrac{1}{4} + \sum_{e=1}^{2} \tfrac{1}{4}[1-(n_{1e}^x)^2-(n_{2e}^x)^2] \right) n_f^x n_f^y \right.\right. \\
& \left.\left. - \sum_{e=1}^{2} \tfrac{1}{4}(n_{1e}^x n_{1e}^y + n_{2e}^x n_{2e}^y)[1-(n_f^y)^2] + \sum_{e=1}^{2} \tfrac{1}{4}(n_{1e}^x n_{1e}^z + n_{2e}^x n_{2e}^z) n_f^y n_f^z \right] \right\} u_i^x \\
& + \sum_{i=1}^{8} \left\{ N_i + \sum_{e=1}^{3} \frac{N_e}{2} [1-(n_{1e}^y)^2-(n_{2e}^y)^2] + \sum_{f=1}^{3} N_f \left[\sum_{e=1}^{2} \tfrac{1}{4}(n_{1e}^x n_{1e}^y + n_{2e}^x n_{2e}^y) n_f^x n_f^y \right.\right. \\
& \left.\left. + \left(-\tfrac{1}{4} + \sum_{e=1}^{2} \tfrac{1}{4}[1-(n_{1e}^y)^2-(n_{2e}^y)^2] \right)[1-(n_f^y)^2] + \sum_{e=1}^{2} \tfrac{1}{4}(n_{1e}^y n_{1e}^z + n_{2e}^y n_{2e}^z) n_f^y n_f^z \right] \right\} u_i^y \\
& + \sum_{i=1}^{8} \left\{ -\sum_{e=1}^{3} \frac{N_e}{2} (n_{1e}^y n_{1e}^z + n_{2e}^y n_{2e}^z) + \sum_{f=1}^{3} N_f \left[\sum_{e=1}^{2} \tfrac{1}{4}(n_{1e}^x n_{1e}^z + n_{2e}^x n_{2e}^z) n_f^x n_f^y \right.\right. \\
& \left.\left. - \sum_{e=1}^{2} \tfrac{1}{4}(n_{1e}^y n_{1e}^z + n_{2e}^y n_{2e}^z)[1-(n_f^y)^2] - \left(-\tfrac{1}{4} + \sum_{e=1}^{2} \tfrac{1}{4}[1-(n_{1e}^z)^2-(n_{2e}^z)^2] \right) n_f^y n_f^z \right] \right\} u_i^z
\end{aligned}
$$

$$+\sum_{i=9}^{20}\left(N_i n_{1i}^y+\sum_{f=1}^{2}\frac{N_f}{2}\{-n_{1i}^x n_f^x n_f^y+n_{1i}^y[1-(n_f^y)^2]-n_{1i}^z n_f^y n_f^z\}\right)u_i^{n1}$$

$$+\sum_{i=9}^{20}\left(N_i n_{2i}^y+\sum_{f=1}^{2}\frac{N_f}{2}\{-n_{2i}^x n_f^x n_f^y+n_{2i}^y[1-(n_f^y)^2]-n_{2i}^z n_f^y n_f^z\}\right)u_i^{n2}+\sum_{i=21}^{26}(N_i n_i^y)u_i^n, \tag{47}$$

$$u^z=\sum_{i=1}^{8}\left\{-\sum_{e=1}^{3}\frac{N_e}{2}(n_{1e}^x n_{1e}^z+n_{2e}^x n_{2e}^z)+\sum_{f=1}^{3}N_f\left[-\left(-\tfrac{1}{4}+\sum_{e=1}^{2}\tfrac{1}{4}[1-(n_{1e}^x)^2-(n_{2e}^x)^2]\right)n_f^x n_f^z\right.\right.$$

$$\left.\left.+\sum_{e=1}^{2}\tfrac{1}{4}(n_{1e}^x n_{1e}^y+n_{2e}^x n_{2e}^y)n_f^y n_f^z-\sum_{e=1}^{2}\tfrac{1}{4}(n_{1e}^x n_{1e}^z+n_{2e}^x n_{2e}^z)[1-(n_f^z)^2]\right]\right\}u_i^x$$

$$+\sum_{i=1}^{8}\left\{-\sum_{e=1}^{3}\frac{N_e}{2}(n_{1e}^y n_{1e}^z+n_{2e}^y n_{2e}^z)+\sum_{f=1}^{3}N_f\left[\sum_{e=1}^{2}\tfrac{1}{4}(n_{1e}^x n_{1e}^y+n_{2e}^x n_{2e}^y)n_f^x n_f^z\right.\right.$$

$$\left.\left.-\left(-\tfrac{1}{4}+\sum_{e=1}^{2}\tfrac{1}{4}[1-(n_{1e}^y)^2-(n_{2e}^y)^2]\right)n_f^y n_f^z-\sum_{e=1}^{2}\tfrac{1}{4}(n_{1e}^y n_{1e}^z+n_{2e}^y n_{2e}^z)[1-(n_f^z)^2]\right]\right\}u_i^y$$

$$+\sum_{i=1}^{8}\left\{N_i+\sum_{e=1}^{3}\frac{N_e}{2}[1-(n_{1e}^z)^2-(n_{2e}^z)^2]+\sum_{f=1}^{3}N_f\left[\sum_{e=1}^{2}\tfrac{1}{4}(n_{1e}^x n_{1e}^z+n_{2e}^x n_{2e}^z)n_f^x n_f^z\right.\right.$$

$$\left.\left.+\sum_{e=1}^{2}\tfrac{1}{4}(n_{1e}^y n_{1e}^z+n_{2e}^y n_{2e}^z)n_f^y n_f^z+\left(-\tfrac{1}{4}+\sum_{e=1}^{2}\tfrac{1}{4}[1-(n_{1e}^z)^2-(n_{2e}^z)^2]\right)[1-(n_f^z)^2]\right]\right\}u_i^z$$

$$+\sum_{i=9}^{20}\left(N_i n_{1i}^z+\sum_{f=1}^{2}\frac{N_f}{2}\{-n_{1i}^x n_f^x n_f^z-n_{1i}^y n_f^y n_f^z+n_{1i}^z[1-(n_f^z)^2]\}\right)u_i^{n1}$$

$$+\sum_{i=9}^{20}\left(N_i n_{2i}^z+\sum_{f=1}^{2}\frac{N_f}{2}\{-n_{2i}^x n_f^x n_f^z-n_{2i}^y n_f^y n_f^z+n_{2i}^z[1-(n_f^z)^2]\}\right)u_i^{n2}+\sum_{i=21}^{26}(N_i n_i^z)u_i^n, \tag{48}$$

The multivariant shape functions for the $R_2^+P_0$ element can also be derived in a slightly different manner, by first finding out the velocity component tangential to the edge at the mid-edge nodes of the $R_2^+P_0$ element and then using the $Q_2^{(20)}P_0$ element to determine the tangential components of velocity at the mid-face nodes of the $R_2^+P_0$ element.

The velocity component tangential to an edge of an $R_2^+P_0$ element varies linearly along the edge; therefore the velocity at a mid-edge node of an $R_2^+P_0$ element is given by

$$\mathbf{u}_e=u_e^{n1}\mathbf{n}_{1e}+u_e^{n2}\mathbf{n}_{2e}+\sum_{c=1}^{2}\tfrac{1}{2}(\mathbf{u}_c\cdot\mathbf{t}_e)\mathbf{t}_e, \tag{49}$$

where $c=1, 2$ correspond to the corner nodes at the two ends of the edge on which the mid-edge node e is located and $\mathbf{t}_e$ is the unit vector tangential to the edge.

The value of the velocity at the centre of a face of the $Q_2^{(20)}P_0$ element is given by

$$\mathbf{u}_f=-\tfrac{1}{4}\sum_{c=1}^{4}\mathbf{u}_c+\tfrac{1}{2}\sum_{e=1}^{4}\mathbf{u}_e, \tag{50}$$

where $c=1, \ldots, 4$ correspond to the four corner nodes and $e=1, \ldots, 4$ correspond to the four mid-edge nodes associated with the face f.

Using equations (49) and (50), the x-component of the last term in equation (44) is

$$\sum_{i=21}^{26} N_i[u_i^x-(\mathbf{u}_i\cdot\mathbf{n}_i)n_i^x]$$

$$=\sum_{i=21}^{26} N_i[u_i^x-(u_i^x n_i^x+u_i^y n_i^y+u_i^z n_i^z)n_i^x]$$

$$=\sum_{i=21}^{26} N_i\left\{\left[\tfrac{1}{2}\sum_{e=1}^{4}\left(u_e^{n1}n_{1e}^x+u_e^{n2}n_{2e}^x+\tfrac{1}{2}\sum_{c=1}^{2}(u_c^x t_e^x+u_c^y t_e^y+u_c^z t_e^z)t_e^x\right)-\tfrac{1}{4}\sum_{c=1}^{4}u_c^x\right][1-(n_i^x)^2]\right.$$

$$-\left[\tfrac{1}{2}\sum_{e=1}^{4}\left(u_e^{n1}n_{1e}^y+u_e^{n2}n_{2e}^y+\tfrac{1}{2}\sum_{c=1}^{2}(u_c^x t_e^x+u_c^y t_e^y+u_c^z t_e^z)t_e^y\right)-\tfrac{1}{4}\sum_{c=1}^{4}u_c^y\right]n_i^x n_i^y$$

$$\left.-\left[\tfrac{1}{2}\sum_{e=1}^{4}\left(u_e^{n1}n_{1e}^z+u_e^{n2}n_{2e}^z+\tfrac{1}{2}\sum_{c=1}^{2}(u_c^x t_e^x+u_c^y t_e^y+u_c^z t_e^z)t_e^z\right)-\tfrac{1}{4}\sum_{c=1}^{4}u_c^z\right]n_i^x n_i^z\right\}, \tag{51}$$

where t_e^x, t_e^y and t_e^z are respectively the x-, y- and z-components of the unit vector tangential to the edge on which the mid-edge node e is located.

The x-component of velocity at a point inside the $R_2^+ P_0$ element can be obtained by collecting the terms for each degree of freedom in equations (44) and (51):

$$u^x=\sum_{i=1}^{8}\left[N_i-\sum_{f=1}^{3}\frac{N_f}{4}[1-(n_f^x)^2]+\sum_{e=1}^{3}\left(\frac{N_e}{2}[1-(n_{1e}^x)^2-(n_{2e}^x)^2]\right.\right.$$

$$\left.+\sum_{f=1}^{2}\frac{N_f}{4}\{(t_e^x)^2[1-(n_f^x)^2]-t_e^x t_e^y n_f^x n_f^y-t_e^x t_e^z n_f^x n_f^z\}\right)\Bigg]u_i^x$$

$$+\sum_{i=1}^{8}\left[\sum_{f=1}^{3}\frac{N_f}{4}n_f^x n_f^y+\sum_{e=1}^{3}\left(-\frac{N_e}{2}(n_{1e}^x n_{1e}^y+n_{2e}^x n_{2e}^y)\right.\right.$$

$$\left.+\sum_{f=1}^{2}\frac{N_f}{4}\{t_e^x t_e^y[1-(n_f^x)^2]-(t_e^y)^2 n_f^x n_f^y-t_e^y t_e^z n_f^x n_f^z\}\right)\Bigg]u_i^y$$

$$+\sum_{i=1}^{8}\left[\sum_{f=1}^{3}\frac{N_f}{4}n_f^x n_f^z+\sum_{e=1}^{3}\left(-\frac{N_e}{2}(n_{1e}^x n_{1e}^z+n_{2e}^x n_{2e}^z)\right.\right.$$

$$\left.+\sum_{f=1}^{2}\frac{N_f}{4}\{t_e^x t_e^z[1-(n_f^x)^2]-t_e^y t_e^z n_f^x n_f^y-(t_e^z)^2 n_f^x n_f^z\}\right)\Bigg]u_i^z$$

$$+\sum_{i=9}^{20}\left(N_i n_{1i}^x+\sum_{f=1}^{2}\frac{N_f}{2}\{n_{1i}^x[1-(n_f^x)^2]-n_{1i}^y n_f^x n_f^y-n_{1i}^z n_f^x n_f^z\}\right)u_i^{n1}$$

$$+\sum_{i=9}^{20}\left(N_i n_{2i}^x+\sum_{f=1}^{2}\frac{N_f}{2}\{n_{2i}^x[1-(n_f^x)^2]-n_{2i}^y n_f^x n_f^y-n_{2i}^z n_f^x n_f^z\}\right)u_i^{n2}+\sum_{i=21}^{26}(N_i n_i^x)u_i^n. \tag{52}$$

Similarly, the y- and z-components of velocity within an $R_2^+ P_0$ element are

$$
\begin{aligned}
u^y = &\sum_{i=1}^{8}\Bigg[\sum_{f=1}^{3}\frac{N_f}{4}n_f^x n_f^y + \sum_{e=1}^{3}\Bigg(-\frac{N_e}{2}(n_{1e}^x n_{1e}^y + n_{2e}^x n_{2e}^y)\\
&+\sum_{f=1}^{2}\frac{N_f}{4}\{-(t_e^x)^2 n_f^x n_f^y + t_e^x t_e^y[1-(n_f^y)^2] - t_e^x t_e^z n_f^y n_f^z\}\Bigg)\Bigg]u_i^x\\
&+\sum_{i=1}^{8}\Bigg[N_i - \sum_{f=1}^{3}\frac{N_f}{4}[1-(n_f^y)^2] + \sum_{e=1}^{3}\Bigg(\frac{N_e}{2}[1-(n_{1e}^y)^2-(n_{2e}^y)^2]\\
&+\sum_{f=1}^{2}\frac{N_f}{4}\{-t_e^x t_e^y n_f^x n_f^y + (t_e^y)^2[1-(n_f^y)^2] - t_e^y t_e^z n_f^y n_f^z\}\Bigg)\Bigg]u_i^y\\
&+\sum_{i=1}^{8}\Bigg[\sum_{f=1}^{3}\frac{N_f}{4}n_f^y n_f^z + \sum_{e=1}^{3}\Bigg(-\frac{N_e}{2}(n_{1e}^y n_{1e}^z + n_{2e}^y n_{2e}^z)\\
&+\sum_{f=1}^{2}\frac{N_f}{4}\{-t_e^x t_e^z n_f^x n_f^y + t_e^y t_e^z[1-(n_f^y)^2] - (t_e^z)^2 n_f^y n_f^z\}\Bigg)\Bigg]u_i^z\\
&+\sum_{i=9}^{20}\Bigg(N_i n_{1i}^y + \sum_{f=1}^{2}\frac{N_f}{2}\{-n_{1i}^x n_f^x n_f^y + n_{1i}^y[1-(n_f^y)^2] - n_{1i}^z n_f^y n_f^z\}\Bigg)u_i^{n1}\\
&+\sum_{i=9}^{20}\Bigg(N_i n_{2i}^y + \sum_{f=1}^{2}\frac{N_f}{2}\{-n_{2i}^x n_f^x n_f^y + n_{2i}^y[1-(n_f^y)^2] - n_{2i}^z n_f^y n_f^z\}\Bigg)u_i^{n2} + \sum_{i=21}^{26}(N_i n_i^y)u_i^n, \qquad (53)
\end{aligned}
$$

$$
\begin{aligned}
u^z = &\sum_{i=1}^{8}\Bigg[\sum_{f=1}^{3}\frac{N_f}{4}n_f^x n_f^z + \sum_{e=1}^{3}\Bigg(-\frac{N_e}{2}(n_{1e}^x n_{1e}^z + n_{2e}^x n_{2e}^z)\\
&+\sum_{f=1}^{2}\frac{N_f}{4}\{-(t_e^x)^2 n_f^x n_f^z - t_e^x t_e^y n_f^y n_f^z + t_e^x t_e^z[1-(n_f^z)^2]\}\Bigg)\Bigg]u_i^x\\
&+\sum_{i=1}^{8}\Bigg[\sum_{f=1}^{3}\frac{N_f}{4}n_f^y n_f^z + \sum_{e=1}^{3}\Bigg(-\frac{N_e}{2}(n_{1e}^y n_{1e}^z + n_{2e}^y n_{2e}^z)\\
&+\sum_{f=1}^{2}\frac{N_f}{4}\{-t_e^x t_e^y n_f^x n_f^z - (t_e^y)^2 n_f^y n_f^z + t_e^y t_e^z[1-(n_f^z)^2]\}\Bigg)\Bigg]u_i^y\\
&+\sum_{i=1}^{8}\Bigg[N_i - \sum_{f=1}^{3}\frac{N_f}{4}[1-(n_f^z)^2] + \sum_{e=1}^{3}\Bigg(\frac{N_e}{2}[1-(n_{1e}^z)^2-(n_{2e}^z)^2]\\
&+\sum_{f=1}^{2}\frac{N_f}{4}\{-t_e^x t_e^z n_f^x n_f^z - t_e^y t_e^z n_f^y n_f^z + (t_e^z)^2[1-(n_f^z)^2]\}\Bigg)\Bigg]u_i^z\\
&+\sum_{i=9}^{20}\Bigg(N_i n_{1i}^z + \sum_{f=1}^{2}\frac{N_f}{2}\{-n_{1i}^x n_f^x n_f^z - n_{1i}^y n_f^y n_f^z + n_{1i}^z[1-(n_f^z)^2]\}\Bigg)u_i^{n1}\\
&+\sum_{i=9}^{20}\Bigg(N_i n_{2i}^z + \sum_{f=1}^{2}\frac{N_f}{2}\{-n_{2i}^x n_f^x n_f^z - n_{2i}^y n_f^y n_f^z + n_{2i}^z[1-(n_f^z)^2]\}\Bigg)u_i^{n2} + \sum_{i=21}^{26}(N_i n_i^z)u_i^n. \qquad (54)
\end{aligned}
$$

Using the following identities for three orthonormal vectors $\mathbf{n}_1$, $\mathbf{n}_2$ and $\mathbf{n}_3$,

$$(n_1^\alpha)^2+(n_2^\alpha)^2+(n_3^\alpha)^2=1, \quad \alpha=x, y, z, \tag{55}$$

$$n_1^\alpha n_1^\beta+n_2^\alpha n_2^\beta+n_3^\alpha n_3^\beta=0, \quad \alpha, \beta=x, y, z, \quad \alpha\neq\beta, \tag{56}$$

where n_i^x, n_i^y and n_i^z are respectively the x-, y- and z-components of the unit vector $\mathbf{n}_i$, it can be easily shown that the multivariant shape functions given in equations (46)–(48) are identical to the multivariant shape functions given in equations (52)–(54) respectively.

Using the shape functions introduced in Sections 3–6, we have developed FEM programmes to simulate viscous incompressible flows using the Q_1P_0, $Q_1^+P_0$ and $R_2^+P_0$ elements. These programmes are used in the remainder of this paper to explore the inherent characteristics of the three types of finite elements.

7. DEVELOPING FLOWS

An example of developing flow is the flow through a long thin tube coming out of an opening at the bottom of a large tank. In this section the performance of the Q_1P_0, $Q_1^+P_0$ and $R_2^+P_0$ elements in simulating a developing flow in a circular channel is investigated. Figure 4 shows the finite element mesh used to analyse the developing flow in a circular channel. The radius of the cross-section of the channel is 1 cm and the length of the channel is 6 cm. The velocity profile is flat at the entrance. Owing to the no-slip condition, the velocity is zero at the lateral surface of the channel. The flow is completely developed before the exit is reached. For the developed flow at the exit the traction force is specified to be zero in the down-channel direction. Zero velocity across the channel is the boundary conditon used in the remaining two directions at the exit. The fluid used is low-density polyethylene (Table I).

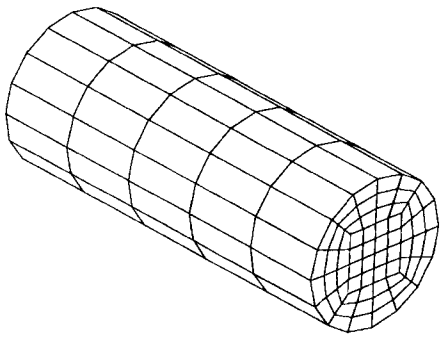

Figure 4. Finite element discretization of a circular channel

Table I. Material properties of low-density Polyethylene (LDPE), wire-covering grade[13]

Reference viscosity μ_0	2000 N s m^{-2}
Reference strain rate ε_e	1·0 s^{-1}
Temperature coefficient of viscosity b_T	0·01 °C^{-1}
Power law index n	0·48
Density ρ	750 kg m^{-3}

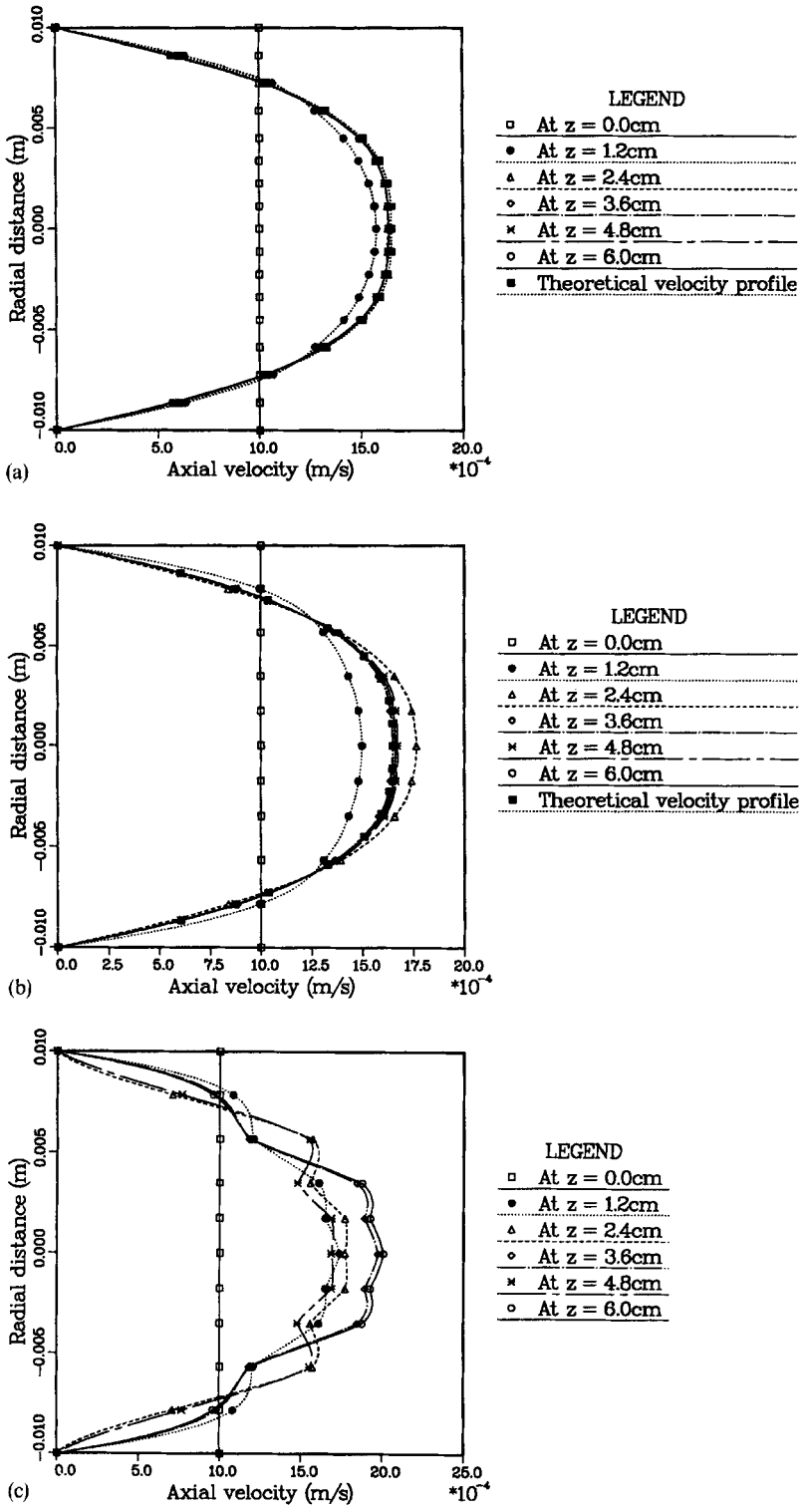

Figure 5. Development of axial velocity along a circular channel using (a) $R_2^+ P_0$, (b) $Q_1^+ P_0$ and (c) $Q_1 P_0$ elements (theoretical velocity profile from Reference 14)

Figures 5(a)–5(c) present the velocity profiles along the diameter of the circular channel at six different locations, using the $R_2^+ P_0$, $Q_1^+ P_0$ and $Q_1 P_0$ elements respectively. As expected physically, the $R_2^+ P_0$ elements give a progressively developing velocity profile. The fully developed velocity profile also matches very well with the velocity profile obtained analytically.[14]

The $Q_1^+ P_0$ elements also give a fully developed velocity profile which is very close to the analytically obtained velocity profile, but the calculated velocity profile overshoots the fully developed velocities before finally dropping back to the developed profile. Using the boundary conditions given earlier, the $Q_1 P_0$ element failed to simulate the developing flow and exhibited oscillations in the velocity profile throughout the channel. The pressure distribution in the circular channel obtained using the $Q_1 P_0$ elements is found to suffer from the checkerboard pressure mode (Figure 6), but the pressure variation obtained by averaging over the neighbouring $Q_1 P_0$ elements is very close to the analytical result (Figure 7). The $R_2^+ P_0$ element gives a linear pressure distribution in most of the channel except near the entrance. The small deviation in the pressure distribution near the entrance is due to the developing velocity profile. The pressure obtained from the $Q_1^+ P_0$ elements is also very close to the analytical value but shows some deviation from the linear distribution owing to the developing nature of the flow.

We have also done a similar analysis for a developing flow through a channel with a rectangular cross-section.[15] Even for simulating a developing flow through a rectangular channel, the three types of finite elements perform in a manner very similar to that observed for the developing flow in a circular channel.

The discrepancy in the behaviour of the different elements in simulating developing flows is due to the discontinuity in the boundary condition at the channel entrance. Owing to the no-slip condition, immediately beyond the entrance the fluid velocity at the wall changes from the uniform velocity at the entrance to zero. As presented in the next section, similar discontinuities can occur in many other problems. A possible cure is also presented in the next section.

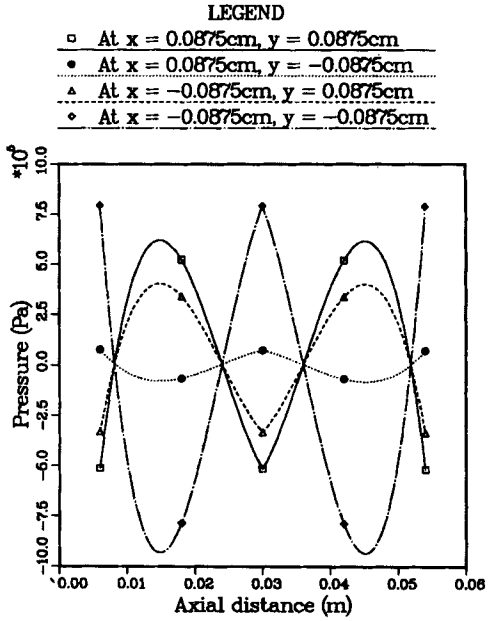

Figure 6. Pressure variation along a circular channel using $Q_1 P_0$ elements

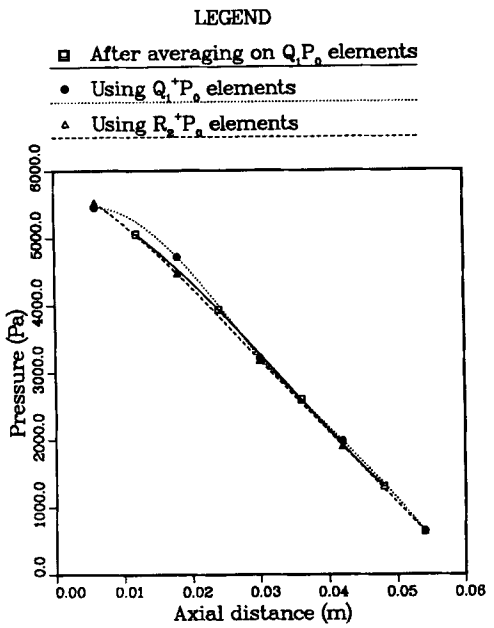

Figure 7. Pressure variation along a circular channel

8. DISCONTINUITIES IN BOUNDARY CONDITIONS

It is evident from the discussion in the last section that discontinuities in the boundary conditions may lead to disturbances in the calculated velocity field obtained by using the Q_1P_0 element. Of course, in real life there are no such discontinuities in the boundary conditions. The singularity at the entrance of the channels in the developing flow simulations originates from the no-slip condition at the lateral boundaries and the uniform velocity boundary condition imposed at the inlet. The singularity can be removed by relaxing either of these idealizations. Using the Q_1P_0 elements, developing flow in channels can be simulated with reasonable accuracy if the no-slip condition is relaxed at the nodes next to the entrance at the lateral boundaries. With the velocity at this layer of nodes at the lateral boundaries specified to be half of the uniform velocity at the inlet, the velocity development along the circular channel is shown in Figure 8. With these new boundary conditions the velocity profile near the entrance is not very accurate, but the velocity distribution farther away from the entrance is quite accurate. The developing flow can also be simulated using the Q_1P_0 elements if the uniform velocity profile at the inlet is modified to force the no-slip boundary condition on the lateral boundary. The velocity development along the circular channel with the modified entrance velocity profile is shown in Figure 9. It shows some fluctuations before converging to the power-law velocity profile. A much stronger influence of the discontinuous boundary conditions is experienced in the next example on the drag flow across a rectangular channel.

8.1. Drag flow across a rectangular channel

In this subsection the cross-channal drag flow caused by a plate moving on top of a rectangular channel is analysed. Two types of finite element meshes used to analyse the flow are shown in

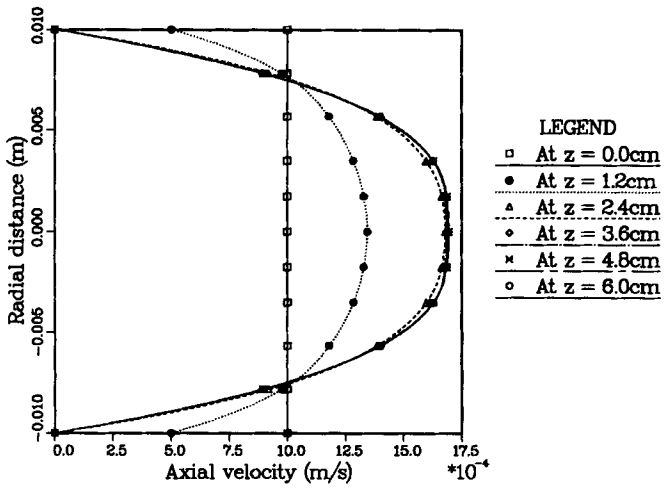

Figure 8. Development of axial velocity along a circular channel using $Q_1 P_0$ elements with partially relaxed no-slip condition

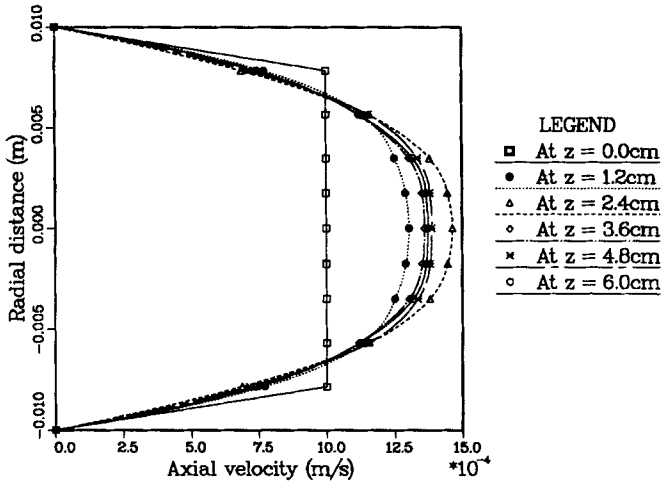

Figure 9. Development of axial velocity along a circular channel using $Q_1 P_0$ elements

Figure 10. The first mesh is a uniform mesh, whereas the second mesh is a non-uniform mesh with finer elements at the two top corners where the velocity and pressure gradients are maximum. At the top corners the boundary conditions are discontinuous. Since the side walls are stationary, the velocity is specified to be zero on the top corners, whereas the particles at the neighbouring nodes on the top moving plate have the same velocity as that of the moving plate owing to the no-slip condition. At the two open sides, assuming a fully developed flow, the velocity component along the channel and the two components of the traction force normal to the axis of the channel are specified to be zero.

For the cross-channel drag flow the velocity distributions across the rectangular channel obtained by using a non-uniform mesh of $Q_1^+ P_0$ and $R_2^+ P_0$ elements are shown in Figures 11(a)

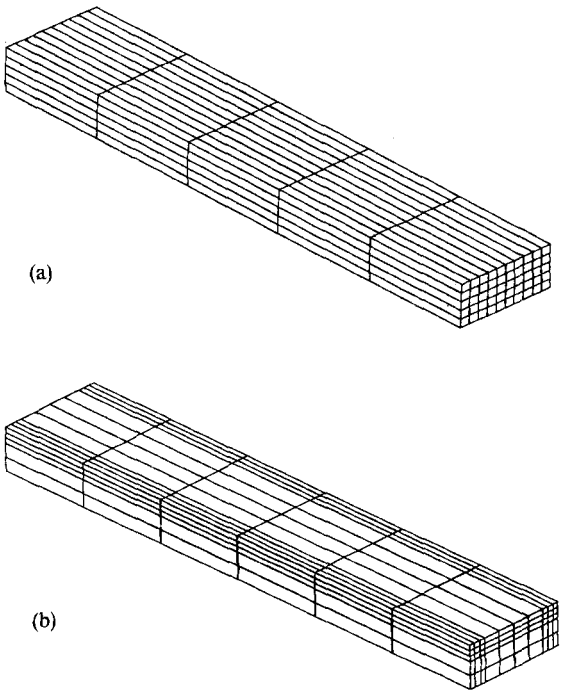

Figure 10. Finite element discretization of a rectangular channel: (a) uniform mesh; (b) non-uniform mesh

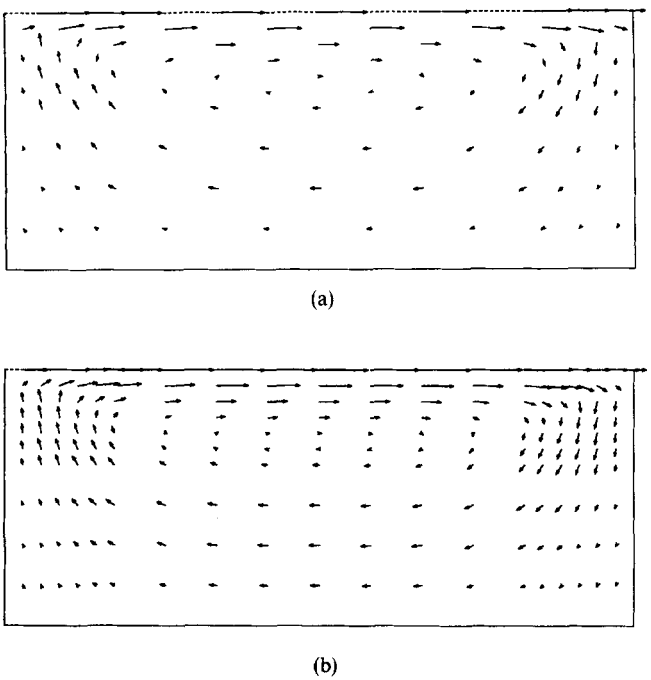

Figure 11. Velocity field across the channel for cross-channel drag flow using (a) $Q_1^+ P_0$ and (b) $R_2^+ P_0$ elements

and 11(b) respectively. The corresponding pressure contours are shown in Figures 12 (a) and 12(b) respectively. The velocity distributions in Figure 11 and the pressure contours in Figure 12 are as expected for the cross-channel drag flow. For the cross-channel drag flow there are singularities at the top corners. The pressure changes from $-\infty$ to ∞ from one end to the other. In the cross-channel flow simulation using the Q_1P_0 element these singularities generate very strong disturbances inside the flow domain. On the non-uniform mesh of Q_1P_0 elements, with 14 elements on the driven side (the top plate) and seven elements on each of the two remaining sides, the velocities obtained do not even satisfy the constant-velocity boundary condition at the top surface and the zero-velocity boundary condition at the three remaining sides for the normal blasting factor (Reference 16, pp. 195–196) of 10^{10} used for forcing the boundary conditions by the blasting technique (Figure 13(a)). As the blasting factor is increased, the boundary conditions are largely satisfied, but then the velocity at some nodes in the flow domain is found to be as large as 10^4 cm s^{-1} for the top plate drag velocity of 2·688 97 cm s^{-1}. The velocity distribution obtained with a uniform mesh with the same number of Q_1P_0 elements (Figure 13(b)) is no better. The pressure distributions obtained on the non-uniform and uniform meshes for the cross-channel drag flows suffer from the checkerboard pressure mode (Figures 14(a) and 14(b)). The small rectangular cells in these pressure contours are due to the very high and very low pressures on the neighbouring elements. Even the pressure contours obtained after averaging the pressure over the neighbouring elements are not satisfactory (Figures 15(a) and 15(b)). In Figures 15(a) and 15(b), before plotting the contours, the pressure values at the corners, which are obtained by averaging over only two elements and are still afflicted with the checkerboard pressure mode, have been discarded.

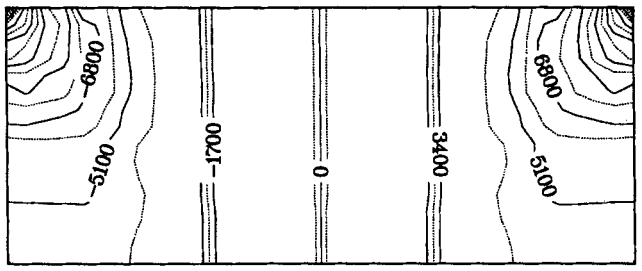

(a)

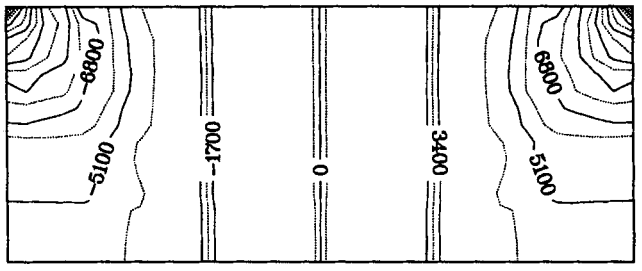

(b)

Figure 12. Pressure contours across the channel for cross-channel drag flow using (a) $Q_1^+P_0$ and (b) $R_2^+P_0$ elements

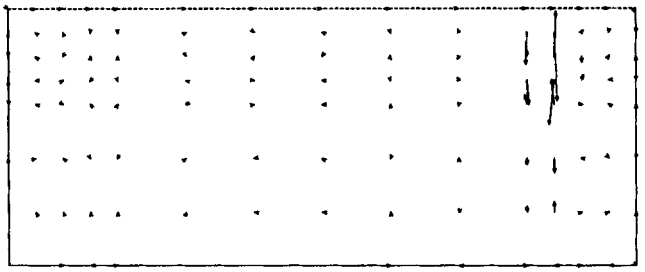

(a)

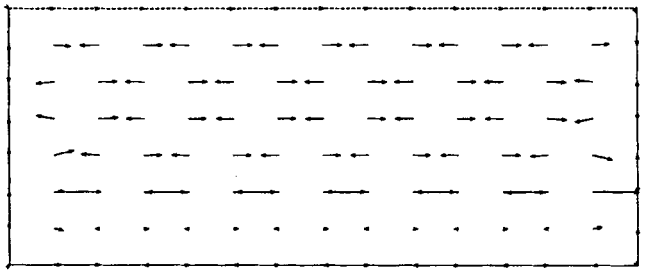

(b)

Figure 13. Velocity distribution across the channel for cross-channel drag flow using Q_1P_0 elements with (a) a non-uniform mesh and (b) a uniform mesh

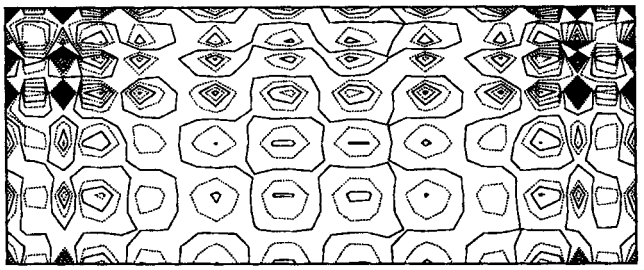

(a)

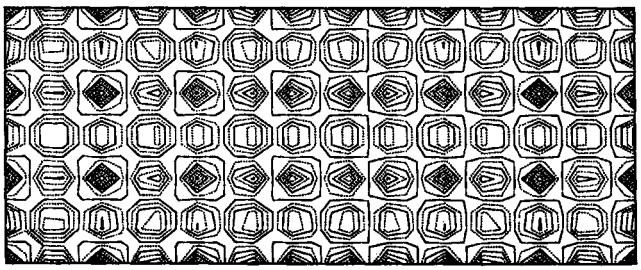

(b)

Figure 14. Pressure contours across the channel for cross-channel drag flow using Q_1P_0 elements with (a) a non-uniform mesh and (b) a uniform mesh

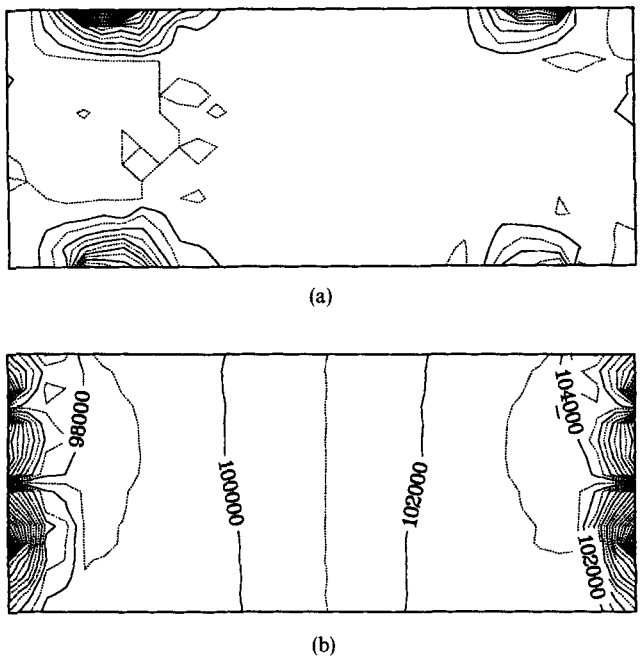

Figure 15. Pressure contours across the channel for cross-channel drag flow after averaging over $Q_1 P_0$ elements using (a) a non-uniform mesh and (b) a uniform mesh

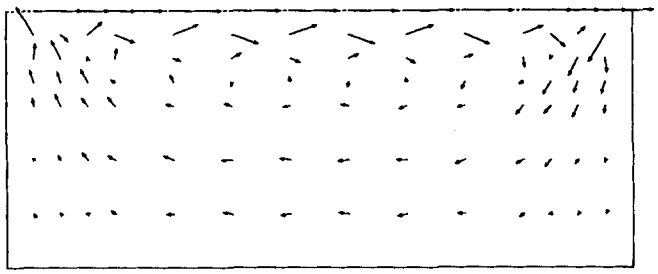

Figure 16. Velocity distribution across the channel for cross-channel drag flow using a non-uniform mesh with 15 $Q_1 P_0$ elements on the driven side

It was shown analytically by Sani *et al.*[3] that two-dimensional cross-channel drag flow with zero velocity specified at the top corners is not a well-posed problem for an even number of elements on the driven side. The cross-channel drag flow problem with zero velocity at the top corners is a well-posed problem if an odd number of elements are used on the driven side and the first and last elements have the same length. Figure 16 shows the velocity distribution for the cross-channel drag flow obtained by using 15 $Q_1 P_0$ elements on the driven side. The velocity distribution in Figure 16 shows some fluctuations but is close to the velocity distribution obtained by using the $Q_1^+ P_0$ and $R_2^+ P_0$ elements. The pressure distribution obtained by using 15 $Q_1 P_0$ elements on the driven side also suffers from the checkerboard pressure mode (Figure 17(a)),

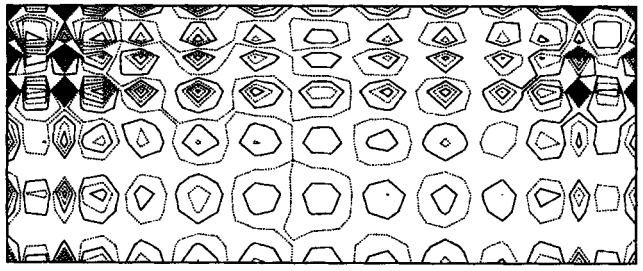

(a)

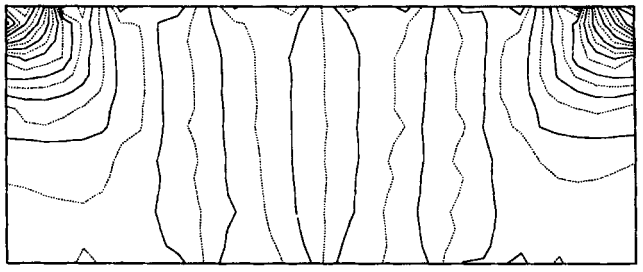

(b)

Figure 17. Pressure contours across the channel for cross-channel drag flow using a non-uniform mesh with 15 Q_1P_0 elements on the driven side: (a) with checkerboard pressure mode; (b) after averaging over the neighbouring elements

but the checkerboard pressure mode is eliminated by averaging the pressure over the neighbouring elements (Figure 17(b)).*

The trick for simulating cross-channel drag flow using an even number of Q_1P_0 elements on the driven side is similar to the remedy used for simulating developing flows, i.e. flatten the discontinuities in the boundary conditions or allow leakage flow at the top corners. In the first case the no-slip condition is partially relaxed at the nodes on the top plate next to the top corners. On these nodes the velocity is specified as half of the top plate velocity. The remaining boundary conditions are the same as used before. With these new boundary conditions the velocity distribution obtained is shown in Figure 18. The velocity distribution is very close to the velocity distributions obtained by using the $Q_1^+P_0$ and $R_2^+P_0$ elements (Figures 11(a) and 11(b)). Even with the new boundary conditions the pressure distribution obtained suffers from the checkerboard pressure mode (Figure 19(a)). The pressure contours obtained after averaging over the neighbouring elements are shown in Figure 19(b). The pressure values at the four corners have been discarded before plotting the pressure contours, as before. With the new boundary conditions the pressure contours obtained after averaging the pressure over the neighbouring Q_1P_0 elements are very close to the pressure contours obtained by using the $Q_1^+P_0$ and $R_2^+P_0$ elements (Figures 12(a) and 12(b)).

If leakage flow is allowed at the top corners by specifying the top plate velocity at the corner nodes, the Q_1P_0 elements successfully simulate the cross-channel drag flow. Figure 20 shows the

* A volume-weighting scheme[3] has been used to obtain the pressure values in Figures 17(b), 19(b) and 21(b).

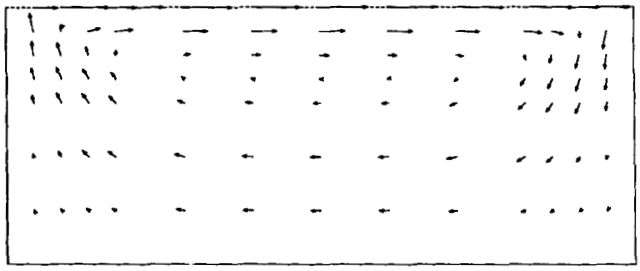

Figure 18. Velocity distribution across the channel for cross-channel drag flow using a non-uniform mesh of Q_1P_0 elements with the no-slip condition partially relaxed at the top corners

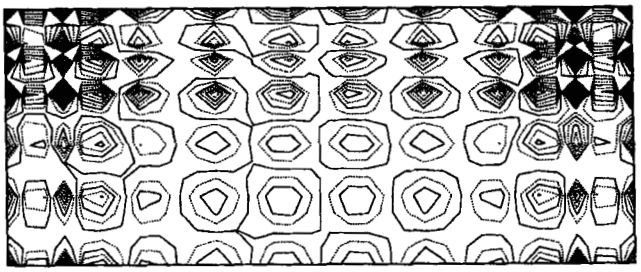

(a)

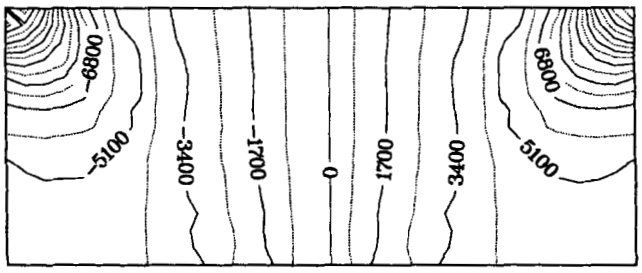

(b)

Figure 19. Pressure contours across the channel for cross-channel drag flow using Q_1P_0 elements with the no-slip condition partially relaxed at the top corners: (a) with checker board pressure mode; (b) after averaging over the neighbouring elements

velocity distribution obtained by using the Q_1P_0 elements for the cross-channel drag flow with leakage flow at the top corners. Even with the leakage flow the pressure distribution for the cross-channel drag flow obtained from the Q_1P_0 elements is afflicted with the checkerboard pressure mode (Figure 21(a)). The pressure distribution obtained after taking a weighted average of the pressure over the neighbouring Q_1P_0 elements is shown in Figure 21(b). The pressure values at the four corner nodes, which are obtained by averaging the pressure on the two neighbouring Q_1P_0 elements only, are still afflicted with the checkerboard pressure mode. These pressure values at the four corners have been discarded before plotting the contours in Figure 21(b). That is why in Figure 21(b) the extreme values of pressure are not at the top corners. The velocity and pressure distributions for the cross-channel drag flow with leakage flow obtained by using the $Q_1^+P_0$ and $R_2^+P_0$ elements are shown in Figures 22 and 23 respectively.

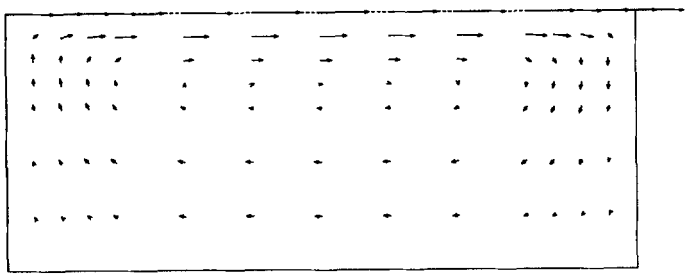

Figure 20. Velocity distribution across the channel for cross-channel drag flow with leakage flow at the top corners using $Q_1 P_0$ elements

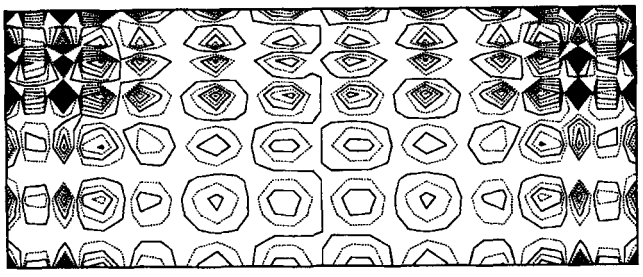

(a)

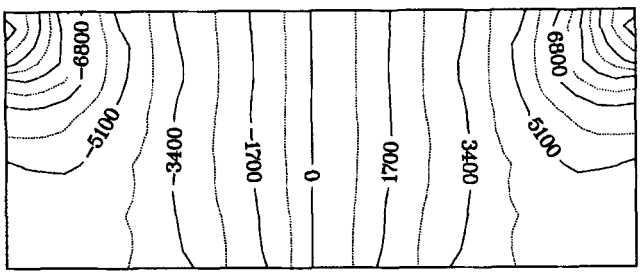

(b)

Figure 21. Pressure contours across the channel for cross-channel drag flow using $Q_1 P_0$ elements with leakage flow at the top corners: (a) with checkerboard pressure mode; (b) after averaging over the neighbouring elements

9. CONCLUSIONS

Univariant elements, which have three degrees of freedom (two degrees in the two-dimensional case) at all velocity nodes, have identical variations for all the velocity components. Accordingly, the value of a velocity component within a univariant element depends only upon the nodal values of the same velocity component. For multivariant elements, which have restricted degrees of freedom at some nodes, different components vary differently within the element. The shape functions for the multivariant elements $Q_1^+ P_0$ and $R_2^+ P_0$ were introduced in Sections 4 and 6 respectively. In contrast to the univariant elements, for multivariant elements each velocity

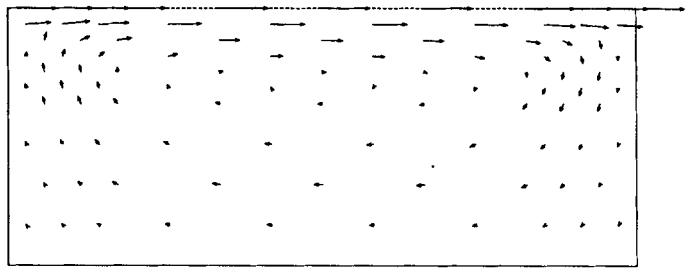

(a)

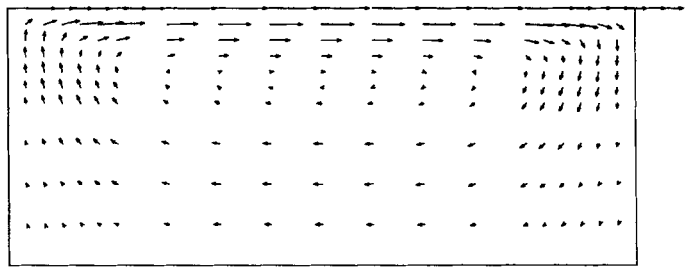

(b)

Figure 22. Velocity distribution across the channel for cross-channel drag flow with leakage flow at the top corners using (a) $Q_1^+ P_0$ and (b) $R_2^+ P_0$ elements

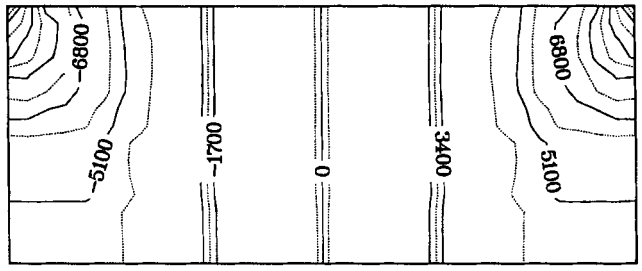

(a)

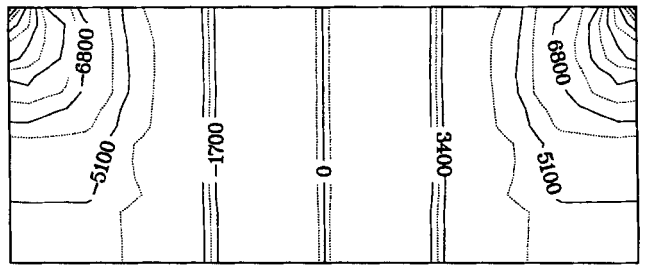

(b)

Figure 23. Pressure contours across the channel for cross-channel drag flow with leakage flow at the top corners using (a) $Q_1^+ P_0$ and (b) $R_2^+ P_0$ elements

component within an element depends upon the values of all the independent velocity components at the nodes of the element.

The pressure distribution obtained from the Q_1P_0 element, which does not satisfy the Babuška–Brezzi condition, is afflicted with the checkerboard pressure mode. Over the uniform finite element meshes used, the checkerboard pressure mode coud be eliminated by taking a weighted average of the pressure over the neighbouring Q_1P_0 elements. The pressure distributions obtained from the $Q_1^+P_0$ and $R_2^+P_0$ elements, which satisfy the Babuška–Brezzi conditions, are free from spurious pressure modes.

If the Q_1P_0 element is used to simulate flows having discontinuous boundary conditions, singularities at the boundaries may propagate disturbance in the complete flow domain, giving completely erroneous velocity and pressure distributions. The velocity distribution for the flow with discontinuous boundary conditions obtained by using the $Q_1^+P_0$ element shows some disturbances, but the fluctuations are restricted to a small region near the singular points. On the other hand, the use of the $R_2^+P_0$ element to simulate flows with discontinuous boundary conditions gives very accurate velocity distributions free from fluctuations. Flows with discontinuous boundary conditions were successfully simulated by partially relaxing the no-slip condition on the Q_1P_0 elements near the singular points.

ACKNOWLEDGEMENTS

We wish to thank San Diego Supercomputer Center for making their computing resources available to us. The authors are also thankful to Professor V. Sernas, Dr. M. Karwe, Dr. S. Gopalakrishna, M. Esseghir and T. Sastrohartono for discussions throughout this work. This work was partially supported by a grant from NJ Center for Advanced Food Technology (CAFT) at Rutgers University.

REFERENCES

1. P. Hood and C. Taylor, 'Navier–Stokes equations using mixed finite element method in flow problems', *Int. Symp. on Finite Element Method in Flow Problems*, Swansea, 1974. UAH Press, Huntsville, pp. 121–132.
2. C. Taylor and P. Hood, 'A numerical solution of the Navier–Stokes equations using FEM technique', *Comput. Fluids*, **1**, 73–100 (1973).
3. R. Sani, P. M. Gresho, R. L. Lee, D. F. Griffiths and M. Engleman, 'The cause and cure (?) of the spurious pressures generated by certain FEM solutions of incompressible Navier–Stokes equations', *Int. j. numer. methods fluids*, **1**, 17–43, 171–204 (1981).
4. F. Brezzi and R. S. Falk, 'Stability of higher order Hood–Taylor methods', *Preprint*, 1990.
5. R. Stenberg, 'Error analysis of some finite element methods for the Stokes problem', *Preprint*, 1990.
6. I. Babuška, 'Error bounds for finite element method', *Numer. Math*, **16**, 322–333 (1971).
7. F. Brezzi, 'On the existence, uniqeness and approximation of saddle point problems arising from Lagrangian multipliers', *RAIRO, Anal. Numer.*, **8**, 129–151 (1974).
8. M. Fortin, 'Old and new finite elements for incompressible flows', *Int. j. numer. methods fluids*, **1**, 347–364 (1981).
9. M. Fortin, 'An analysis of the convergence of mixed finite element methods', *RAIRO, Anal, Numer.*, **11**, 341–354 (1977).
10. V. Girault and P. A. Raviart, *Finite Element Methods for Navier–Stokes Equations*, Springer, Berlin, 1986.
11. J. J. Connor and C. A. Brebbia, *Finite Element Techniques for Fluid Flow*, Newnes–Butterworths, London/New York, 1977.
12. O. C. Zienkiewicz, *The Finite Element Method*, McGraw-Hill, New York, 1971.
13. R. T. Fenner, *Principles of Polymer Processing*, Chemical Publishing, New York, 1979.
14. R. B. Bird, R. C. Armstrong and O. Hassager, *Dynamics of Polymeric Liquids, Vol. 1*, Wiley, New York, 1987.
15. M. Gupta, 'Shape functions for multivariant finite elements for 3-dimensional analysis of incompressible flows of non-Newtonian fluids', *Ph.D. Thesis*, Department of Mechanical and Aerospace Engineering, Rutgers University, New Brunswick, NJ, 1990.
16. S. S. Rao, *The Finite Element Method in Engineering*, 2nd edn, Pergamon, New York, 1989.